# Energy dependence of quasi-periodic oscillations in accreting X-ray pulsars

Hemanth Manikantan [1,2]★ Biswajit Paul,[1] Rahul Sharma [1], Pragati Pradhan [3] and Vikram Rana [1]

[1]*Astronomy & Astrophysics Department, Raman Research Institute, CV Raman Avenue, Sadashivanagar, Bangalore 560080, India*
[2]*INAF Istituto di Astrofisica e Planetologia Spaziali, Via del Fosso del Cavaliere 100, I-00133 Roma, Italy*
[3]*Department of Physics, Embry Riddle Aeronautical University, Prescott Campus, 3700 Willow Creek Road, Prescott, AZ 86301, USA*

## ABSTRACT

We present the results from an investigation of the energy dependence of quasi-periodic oscillations (QPOs) exhibited by accreting X-ray pulsars using data from archival *XMM-Newton*, *NuSTAR*, *RXTE*, and *NICER* observations. In a search for the presence of QPOs in 99 *XMM-Newton* and *NuSTAR* observations, we detected QPOs in eleven observations of five sources, viz., 4U 1626–67 (48 mHz), IGR J19294+1816 (30 mHz), V 0332+53 (2, 18, and 40 mHz), Cen X–3 (30 mHz), and XTE J1858+034 (180 mHz). A positive correlation of the QPO rms amplitude with energy is exhibited by 4U 1626–67, IGR J19294+1816, Cen X–3 and XTE J1858+034, while no energy dependence is observed in V 0332+53. We also analysed the energy spectrum to decouple thermal (soft-excess) from non-thermal emission and determine if the soft-excess has different QPO properties. We found no evidence for different QPO characteristics of the soft excess. The *NuSTAR* observations of V 0332+53 during the Type-I outburst in 2016 show the presence of twin QPOs at 2.5 and 18 mHz, while the *XMM-Newton* and *NuSTAR* observations during the Type-II outburst in 2015 show a QPO at 40 mHz. We review the observed QPO properties in the context of QPOs found in other types of accreting sources and the models usually used to explain the QPOs in accreting X-ray pulsars.

**Key words:** methods: data analysis – pulsars: general – X-rays: binaries – X-rays: individual: 4U 1626–67, IGR J19294+1816, V 0332+53, Cen X–3, XTE J1858 + 034 – accretion discs.

## 1 INTRODUCTION

Accreting X-ray pulsars (XRPs) are strongly magnetized rotating neutron stars, having surface magnetic fields of the order of $10^{12}$ Gauss, that accretes matter from a binary stellar companion either via Roche lobe overflow or from its strong stellar wind. Quasi-periodic oscillations (QPOs), exhibited as a concentration of Fourier power at frequencies of a few 10 mHz in the power spectral density (PSD), are a transient phenomenon in XRPs. These mHz QPO have been reported in about 20 XRPs (See the list of sources in James et al. 2010 and Raman, Paul & Bhattacharya 2021) in both transient and persistent sources.

The strong magnetic field of the neutron star impedes the formation of an accretion disc inside the magnetospheric radius ($r_M$) at about a few 1000 km from the neutron star. Therefore, the radius of the inner accretion disc is expected to be of the order of $r_M$. QPOs are usually exhibited by XRPs at frequencies of a few 10 mHz, and since the Keplerian orbital frequency of matter around a canonical 1.4 $M_\odot$ neutron star at $r_M \sim 5000$ km is $\frac{1}{2\pi}\sqrt{\frac{GM_{NS}}{r_M^3}} \sim 200$ mHz, the QPOs are qualitatively associated with phenomena related to the inner accretion disc. The QPO is XRPs are usually observed from a few keV up to ∼40 keV (Qu et al. 2005; Raichur & Paul 2008; Nespoli & Reig 2010; Devasia et al. 2011; Raman et al. 2021; Sharma

et al. 2023a), but 1A 0535 + 262 is an exception, where QPO is only present in hard X-rays above ∼25 keV (Finger, Wilson & Harmon 1996; Ma et al. 2022). The accretion disc is considered to be always present in persistent sources. On the contrary, transient sources are believed to have phases of formation of a temporary accretion disc around the neutron star during their luminous phases.

The two most commonly used models to explain QPOs in XRPs are the Magnetospheric beat-frequency model (BFM; Alpar & Shaham 1985) and the Keplerian frequency model (KFM; Klis 1997). BFM models the QPO as a modulation in the mass accretion rate on to the NS poles at the beat frequency between the spin frequency of NS ($\nu_{NS}$) and the orbital frequency of the inner accretion disc. Matter is channelled onto the neutron star from inhomogeneity in the inner accretion disc along the spinning magnetic field lines. According to BFM, $\nu_{QPO} = \nu_k - \nu_{NS}$, where $\nu_k$ is the Keplerian orbital frequency of the inner accretion disc and $\nu_{NS}$ is the spin period of the neutron star. KFM models the QPO as an effect due to the blobs of matter in the inner accretion disc intercepting the emission from the neutron star, because of which the observer perceives a modulation in the X-ray flux. According to KFM, $\nu_{QPO} = \nu_k$. KFM places a constraint on the observed QPO frequency based on the neutron star spin frequency $\nu_{NS} < \nu_{QPO}$, based on the argument of centrifugal inhibition of accreted matter beyond this limit. BFM, on the other hand, provides constraints on the minimum X-ray flux to be maintained by accretion based on the centrifugal inhibition limit (Finger 1998). Assuming the radius of the inner accretion disc also scales by the accretion rate

★ E-mail: hemanth.manikantan@inaf.it

$\dot{M}^{-\frac{2}{7}}$ (and hence the X-ray luminosity), the Keplerian frequency of the inner accretion disc, and thereby the QPO frequency, is expected to increase with luminosity in both KFM and BFM (Finger 1998).

QPOs exhibit variability as a function of photon energy, which puts constraints on the applicable models that explain the origin of QPO. So far no general characteristic trend has been recognized in XRPs with respect to the QPO rms amplitude as a function of energy. Correlation (IGR J19294 + 1816; Raman et al. 2021, KS 1947 + 300; James et al. 2010, XTE J1858 + 034; Mukherjee et al. 2006, LMC X–4; Sharma et al. 2023a), anticorrelation (A 1118–615; Nespoli & Reig 2010, V 0332+53; Qu et al. 2005, Cen X–3 Liu et al. 2022, GX 304–1; Devasia et al. 2011) and no correlation (Cen X–3; Raichur & Paul 2008) have all been reported. Most of the studies mentioned above were performed using *RXTE*/PCA data, which was sensitive to photons in the 2–30 keV energy band. There are also cases where unusual dependency is seen, for instance, the detection of QPO at 80 keV and the convex-shaped relation between QPO rms and photon energy in 1A 0535 + 262 peaking at around 60 keV from the *Insight*/HXMT data which offers 1–250 keV spectral coverage (Ma et al. 2022).

We performed a comprehensive search for QPOs in the archival *XMM-Newton* and *NuSTAR* observations of XRPs. Additional data from *RXTE*/PCA and *NICER* were analysed for 4U 1626–67. In observations where QPO was detected, we constructed the variation of QPO rms as a function of photon energy and analysed the energy spectrum.

The paper is arranged as follows. Section 2 describes the instruments utilized, data reduction, and the methods employed for timing and spectral analyses. The results of the timing and spectral analysis for each source are provided in Section 3. The discussion of findings and interpretation of the results is given in Section 4. The log of all observations utilized in this work and fits on individual power spectral densities are given in Appendices A and B.

## 2 OBSERVATIONS AND DATA REDUCTION

### 2.1 Instruments and data reduction

*XMM-Newton*: The PN-type European Photon Imaging Camera (EPIC-PN) onboard the *X-ray Multi-Mirror Mission* (*XMM-Newton*) is an array of 12 pn-CCDs coupled to focussing optics, sensitive to photons in 0.15–15 keV (Strüder et al. 2001). EPIC-PN has an effective area of around 1000 cm$^2$ at 1.5 keV. We followed the standard data-reduction steps from *XMM-Newton* data analysis threads.[1] First, the event list for the EPIC-PN instrument was generated from the Observation Data Files with the tool epproc, using the calibration files generated with the tool cifbuild. The generated event time stamps were then corrected for the motion of the earth around the barycentre of the solar system using the tool barycen and subsequently filtered for time intervals of high background particle flaring. We also checked the observations for pile-up, following the steps mentioned in SAS Thread *epatplot*.[2] If found, the piled-up data were removed by excluding the central core of the PSF in Imaging mode observations using an annular source region, and by removing the boresight columns in Timing mode observations.[3]

The source and background light curves and spectra were extracted from the resulting events file with the tool evselect. A circular source and annular background region were used for imaging mode observations, while rectangular strips were used for timing mode observations.

*NuSTAR*: *NuSTAR* operating in 3–79 keV consists of two CdZnTe detectors paired to separate hard X-ray focussing optics and have a total effective area of about 1000 cm$^2$ at 10 keV (Harrison et al. 2013). The two detectors are called Focal Plane Modules (FPMs) A and B. We followed the standard data-reduction steps from The NuSTAR Data Analysis Software Guide.[4] using the NuSTAR Data Analysis Software package NuSTARDAS v2.1.1. The filtered and calibrated events files were generated with the tool nupipeline using the NuSTAR calibration data base (CALDB) version 20210315. Using nuproducts, the source and background light curves were generated from circular regions of FPMA and FPMB modules. The light curves from FPMA and FPMB were summed together using task lcmath.

*RXTE*/PCA: The Proportional Counter Array (PCA) on the *Rossi X-ray Timing Explorer* (*RXTE*) consists of five collimated large-area Xenon filled proportional counter units with a total effective area of ∼6500 cm$^2$, sensitive to photons in 2–60 keV (Jahoda et al. 2006). PCA light curves in different energy bands were extracted from the GoodXenon Event mode data files using the tool seextrct using the photon energy to channel conversion table given here.[5] We have used only one *RXTE*/PCA observation (of 4U 1626–67, OID P10101) in this work.

*NICER*: The *Neutron star Interior Composition Explorer* (*NICER*) is an X-ray observatory installed on the International Space Station (ISS). The X-ray Timing Instrument (XTI) onboard *NICER* comprises 56 X-ray concentrator optics coupled to SDD detectors (Gendreau et al. 2016). The XTI operates in the 0.2–10 keV energy range and has an effective area of ∼1900 cm$^2$ at 1.5 keV. XTI light curves in different energy bands were extracted using the tool nicerl3-lc and the spectra were extracted using the tool nicerl3-spect after screening the data from the noisy detectors (DET_ID 14 and 34). The background light curves and spectra were generated using the Space Weather background model. The light curves were corrected for the solar-system barycentre using the tool barycorr. We have only used the *NICER* observations of 4U 1626 − 67 (Table 1) in this work.

### 2.2 Method of analysis

For each observation listed in Table B1, the background-subtracted light curves were generated with a bin size of 1 s. Setting the bin size to 1 s enables the construction of PSD up to 500 mHz, facilitating the ability to check for mHz QPOs. The PSD of each light curve was generated using the XRONOS tool powspec.[6] The light curves were divided into segments of length 4096 s (1024 s for *NICER*) and the power spectra obtained from the light-curve segments were averaged to improve the signal-to-noise ratio of PSD (van der Klis 1989). The resulting PSD was normalized so that it has units of (rms/mean)$^2$ Hz$^{-1}$ so that integrating the PSD over frequency gives the fractional rms squared variability. An expected flat noise level of ∼2/mean was also subtracted from the PSD (van der Klis 1989, Belloni & Hasinger 1990). Normalization of PDS and subtraction of the expected noise

---

[1] https://www.cosmos.esa.int/web/xmm-newton/sas-threads
[2] https://www.cosmos.esa.int/web/XMM-Newton/sas-thread-epatplot
[3] http://xmm-tools.cosmos.esa.int/external/xmm_user_support/documentation/sas_usg/USG/epicpileuptiming.html

[4] https://heasarc.gsfc.nasa.gov/docs/nustar/analysis/nustar_swguide.pdf
[5] https://heasarc.gsfc.nasa.gov/docs/xte/e-c_table.html
[6] https://heasarc.gsfc.nasa.gov/lheasoft/ftools/fhelp/powspec.txt

**Table 1.** Observations catalogue for timing and spectral analysis, of sources with QPO detection.

| Source | Observatory/Instrument | Obs. ID | Observing mode | Start date (Duration in ks) | Avg. count rate† (cts s⁻¹) | Piled-up | Avg. count rate‡ (cts s⁻¹) |
|---|---|---|---|---|---|---|---|
| 4U 1626−67 | XMM-Newton/PN | 0111070201 | PrimeSmallWindow | 24-08-2001 (16) | $33.20 \pm 0.06$ | – | – |
| | | 0152620101 | PrimeSmallWindow | 20-08-2003 (84) | $27.63 \pm 0.02$ | XRL§ | – |
| | RXTE/PCA | P10101 | Good Xenon | 10-02-1996 (395) | $306.90 \pm 0.05$¶ | – | – |
| | NICER/XTI | 6203800 1XX§ | N/A | 28-04-2023 (40)§ | $22.12 \pm 0.04$§ | – | – |
| IGR J19294 + 1816 | XMM-Newton/PN | 0841190101 | PrimeFullWindow | 13-10-2019 (67) | $20.57 \pm 0.03$ | PU | $2.74 \pm 0.09$ |
| V 0332+53 | XMM-Newton/PN | 0763 470 301 | FastTiming | 10-09-2015 (32) | $423.68 \pm 0.19$ | PU | $194.7 \pm 0.1$ |
| | | 0763 470 401 | FastTiming | 16-09-2015 (31) | $280.12 \pm 0.12$ | PU | $162.0 \pm 0.1$ |
| | NuSTAR/FPM | 80102002004 | N/A | 10-09-2015 (15) | $209.40 \pm 0.10$ | – | – |
| | | 80102002006 | N/A | 16-09-2015 (17) | $136.60 \pm 0.10$ | – | – |
| | | 90202031002 | N/A | 30-07-2016 (44) | $24.52 \pm 0.02$‖ | – | – |
| | | 90202031004 | N/A | 31-07-2016 (44) | $19.64 \pm 0.02$‖ | – | – |
| Cen X−3 | XMM-Newton/PN | 0400550201 | FastTiming | 12-06-2006 (80) | $452.10 \pm 0.07$ | No | – |
| XTE J1858 + 034 | NuSTAR/FPM | 90501348002 | N/A | 03-11-2019 (90) | $17.27 \pm 0.02$‖ | – | – |

† Before pile-up correction.
‡ After pile-up correction.
§ This XMM-Newton observation is affected by X-ray loading.
¶ Across all five PCUs of RXTE that were ON during this observation.
‖ In FPMA module.
§: XX = 03, 04, 06, 11, 12, 15–17, 22, 32, 33, 35–42, 45–47, 49. The start date of OID 6 203 800 103 and total on-source exposure across all the observations (out of a total elapsed time duration of 5933 ks) are given. The average count rate in 0.5–10 keV of the combined lightcurve from the observations is given.

level was achieved by setting norm $=-2$ in powspec. The fractional rms amplitude from QPO in *NICER* observations were estimated from non-background-corrected light curves, and hence the estimated QPO fractional rms were corrected for background by scaling it with a factor of $\sqrt{(S+B)}/S$ (Belloni & Hasinger 1990), where $S$ and $B$ are the source and background count rates, respectively.

QPOs appeared as a relatively wide asymmetric bump in the PSD (see Appendix A) and were identified through visual inspection. Apart from QPOs some of the PSDs also showed sharp narrow features (see e.g. Figs A1, A2, A4, and A8) corresponding to the spin period of the pulsar and its harmonics. PSD to a factor of four frequency range on either side of the QPO vicinity ($0.25\nu_{QPO}$–$4\nu_{QPO}$) or a factor of 8 for the low $Q$-factor cases (V 0332+53 and Cen X−3) was fitted with the combination of a powerlaw or lorentzian (for the continuum), and a lorentzian (for the QPO). The sharp spikes in PSD corresponding to the pulsar spin period and its harmonics were removed before performing the fit. The centre ($\nu_{QPO}$), width (width$_{QPO}$) of lorentzian and the integrated fractional rms-squared power under the lorentzian ($P_{rms} \pm \Delta P_{rms}$) was then estimated. Fractional rms amplitude variability of the QPO was estimated as $\sqrt{P_{rms}} \pm (\Delta P_{rms}/2\sqrt{P_{rms}})$. To assess the variation of QPO fractional rms in different energy ranges, the procedure was repeated on PSDs derived from light curves in different energy bands. The errors assigned to the QPO fractional rms values are their 68 per cent ($1\sigma$) confidence intervals and all other parameters are their 90 per cent ($2.7\sigma$) confidence intervals, unless otherwise stated. The fractional rms amplitude for the high-frequency (200 mHz) QPO in XTE J1858 + 034 was assessed after constructing the PSD from light curve with 0.5 s bin size so that the Nyquist frequency is 1 Hz.

We analysed energy-resolved light curves for a total of 99 observations of 29 XRPs and QPOs were identified in eleven of them (Table 1). The very fact that QPOs were not detected in all the observations of a particular source, and in sources which have previous reports of QPO, indicates the transient nature of QPOs in XRPs.

In the observations with a QPO detection, we also performed the spectral analysis. We used the package XSPEC v12.13.1 (Arnaud, Dorman & Gordon 1999) for performing the spectral analysis. Unless stated otherwise, we have binned the spectrum to a minimum of 25 counts per bin.

## 3 SOURCES AND RESULTS

### 3.1 4U 1626 − 67

4U 1626 − 67 is a persistent Low mass Ultra-compact X-ray binary in which a 130 mHz spinning strongly magnetized ($\sim 3 \times 10^{12}$ G) neutron star (Coburn et al. 2002, and references therein) is accreting Oxygen and Neon rich matter from a companion by Roche lobe overflow, that is assessed from the presence of Oxygen/Neon emission complex at 1 keV in its energy spectrum (Schulz et al. 2001). The X-ray spectrum of the persistent accreting pulsar 4U 1626 − 67 has been extensively studied, and it usually exhibits a soft blackbody component along with the power law (Camero-Arranz et al. 2012). A QPO at 48 mHz is well established in the source at multiple wavelengths, in the Optical band with 3 per cent rms amplitude (Chakrabarty 1998), UV band with 3 per cent rms amplitude in the near-UV to 15 per cent in the far-UV (Chakrabarty et al. 2001) and X-ray band with 15 per cent rms (Shinoda et al. 1990, Kaur et al. 2008). The 48 mHz QPO is observed in 4U 1626–67 when the pulsar is spinning down, and lower frequency QPOs (36 and 40
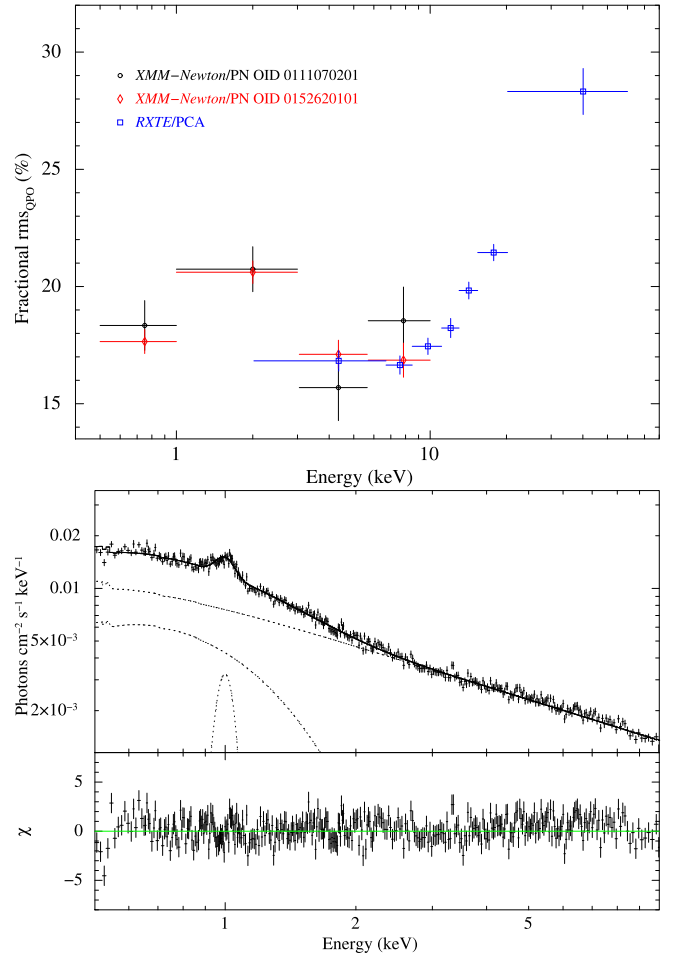


**Figure 1.** Top: The energy dependent variation of QPO fractional rms amplitude in 4U 1626–67 from *XMM-Newton*/PN (red, black) and *RXTE*/PCA (blue) observations. Bottom: The 0.5–10 keV unfolded spectrum and residuals to the best-fit model tbabs * (powerlaw + gaussian + bbody) on the *XMM-Newton* Obs. ID 0111070201. Soft excess was modelled with a black body component of $kT \sim 0.3$ keV.

mHz) are observed when the source is spinning up (see Jain, Paul & Dutta 2010, and references therein).

The 48 mHz QPO is present in two *XMM-Newton* observations (Fig. A1; Beri et al. 2014). To extend the study of QPO variability to higher energy bands, we also selected an *RXTE*/PCA observation having $\sim 147$ ks on-source exposure in which 48 mHz QPO was reported by Kaur et al. (2008). The band-limited noise between 12 and 192 mHz in the PDS of both the *XMM-Newton*/PN observations were fitted with a powerlaw and the QPO at 48 mHz was fitted with a Lorentzian (Fig. A1). The band-limited noise between 12 and 192 mHz in the *RXTE*/PCA observation was fitted with a powerlaw, a broad low frequency Gaussian at $\sim 12$ mHz, a narrow Lorentzian at $\sim 80$ mHz for the QPO-pulsar-sideband (Kommers, Chakrabarty & Lewin 1998), and the QPO at 48 mHz was fitted with a Lorentzian (Fig. A2). We determined the energy-resolved variation of QPO in the 0.5–60 keV energy band (Fig. 1). The fractional rms amplitude of QPO exhibits a steadily rising trend in 3–60 keV, increasing from about 15 per cent to 28 per cent. However, it deviates from this trend below 3 keV, where the QPO rms is high at around 20 per cent in 1–3 keV and 18 per cent in 0.5–1 keV. To study the QPO characteristics below 3 keV in finer energy
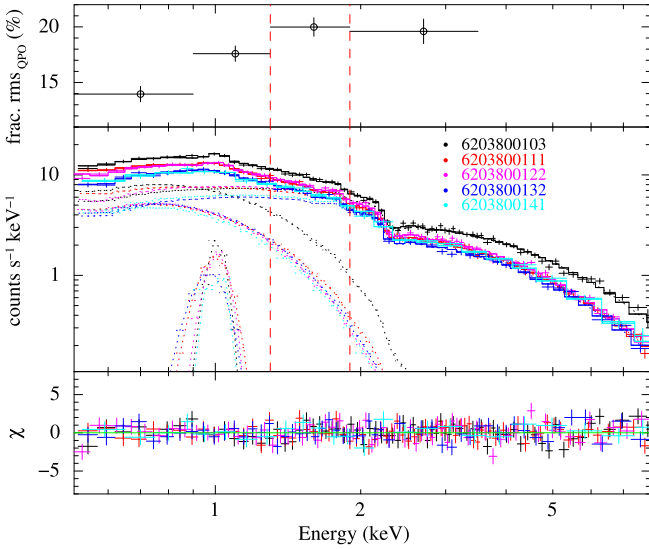
**Figure 2.** The top panel shows QPO fractional rms amplitude in 4U 1626 − 67 in different energy bands from combined PDS of all the *NICER* observations. The middle panel shows the *NICER* photon energy spectrum and the best-fitting composite spectral model `tbabs * (powerlaw + bbody + gaussian)` and the contribution from individual model components, especially the soft excess and the Neon line at 1 keV, on selected five observations. The vertical dashed lines indicate the energy range 1.3–1.9 keV, where the QPO rms peaks (See Section 4.4). The bottom panel shows residuals to the best-fitting spectral model.

segments, we analysed the combined PSD from multiple *NICER* observations (Table 1) of 4U 1626 − 67 having the 48 mHz QPO. The band-limited noise between 12 and 192 mHz in the PDS of *NICER* observation was fitted with a `powerlaw` and the QPO at 48 mHz was fitted with a `Lorentzian` (Fig. A3). We estimated the fractional rms amplitude of the QPO in five energy bands; 0.5–0.9 (14 per cent), 0.9–1.3 (17 per cent), 1.3–1.9 (20 per cent), and 1.9–3.5 keV (19 per cent; Fig. 2). A detailed discussion on the energy dependence of QPO rms below 3 keV, especially from *NICER* observations, is given in Section 4.4.

We analysed the 0.5–10 keV spectra from both *XMM-Newton* observations and the 0.5–8 keV spectra from all the *NICER* observations. We adopted the spectral model from Beri, Paul & Dewangan (2018). A `powerlaw` could fit the continuum, and the strong Neon emission complex at ∼ 1 keV was fitted with a `Gaussian` profile. The spectra also showed the presence of soft excess, which was modelled with a blackbody component of $kT_{BB} \sim 0.3$ keV. The finally used spectral model is `tbabs*(powerlaw+bbody + gaussian)` (Figs 1 and 2). The best-fitting spectral model parameters for all the observations are given in Table 2.

### 3.2 IGR J19294 + 1816

IGR J19294 + 1816 is a transient high mass X-ray binary in which a spinning ($\nu_{spin} \sim$ 83 mHz) strongly magnetized ($\sim 4 \times 10^{12}$ G) neutron star (Tsygankov et al. 2019a) accretes matter from a Be-type companion star (Rodes-Roca et al. 2018) in a 117 d orbit (Rodriguez et al. 2009). QPO was reported in the *AstroSat*/LAXPC observation at 32 mHz during the luminosity decline phase of a Type-I outburst of the source during the periastron passage in 2019 (Domcek et al. 2019; Raman et al. 2021).

We detected QPO in an *XMM-Newton* observation at 30 mHz (Fig. A4) during the rising phase of the same 2019 outburst. The

band-limited noise in PDS between 8 and 128 mHz was fitted with a `powerlaw` and the QPO at 30 mHz was fitted with a `Lorentzian` (Fig. A4). The fractional rms amplitude of QPO shows an increasing trend in the 0.5–10 keV range and the trend continues till 30 keV (Fig. 3), as evident from the results of Raman et al. (2021).

We tried to fit different continuum models to the 0.5–10 keV *XMM-Newton*/PN spectrum and found that `powerlaw*highecut` and `powerlaw*FDcut` gave good fits to the continuum with acceptable values for all the spectral parameters. Residuals left by the iron fluorescence line could be modelled with a `Gaussian` emission profile. Since the width of the `Gaussian` was not constrained by the fit, we fixed it to 10 eV (the spectral resolution of EPIC-PN at 6.4 keV is 150 eV). The finally used spectral model is `tbabs*(powerlaw*highecut + gaussian)` (Fig. 3). The best-fitting spectral model parameters are given in Table 3.

### 3.3 V 0332+53

V 0332+53 is a transient high-mass X-ray binary in which a 227 mHz pulsar accretes matter from a Be-type companion star in a 34 d eccentric ($e \sim 0.3$) orbit (Stella et al. 1985). QPO was discovered in the source during a Type-II outburst in 1989 from *Ginga*/LAC observations by Takeshima et al. (1994) at 51 mHz with about 5 per cent rms in the 2.3–37.2 keV energy band. The 51 mHz QPO and another 220 mHz QPO (centred at the NS spin frequency) were found in later observations during the 2004/2005 Type-II outburst decay phase with *RXTE*/PCA (Qu et al. 2005), and *INTEGRAL*/JEM-X and IBIS (Mowlavi et al. 2006) observations. Qu et al. (2005) also observed that the QPO central frequency does not vary with flux and that the QPO rms stays constant as a function of photon energy till 10 keV and drops beyond 10 keV.

Two quasi-simultaneous observations from *XMM-Newton* and *NuSTAR* during the 2015 Type-II outburst show the presence of a QPO at about 40 mHz (Figs A5 and A6), and two observations from *NuSTAR* during a Type-I outburst in 2016 show twin QPOs at 2.5 mHz and 18 mHz (Fig. A7). The *XMM-Newton*/PN and *NuSTAR* PSDs of the 2015 observations in the 0.005–0.24 Hz range were fitted with a wide `Lorentzian` for the band-limited noise and another narrow `Lorentzian` at 40 mHz for the QPO (Figs A5, A6). The *NuSTAR* PSDs of 2016 observations in the 0.005–0.12 Hz range were fitted with `powerlaw * highecut` for the broad-band noise and two `Lorentzian` profiles at ∼2.5 mHz and ∼18 mHz for the twin QPOs (Fig. A7). The rms amplitude of 40 mHz QPO in the 2015 observations, and the 2.5 mHz and 18 mHz QPO in the 2016 observations does not exhibit any secular trend in energy (Fig. 4). The quality factor of the 2.5 mHz QPO is higher than the 18 and 40 mHz QPOs. The *NuSTAR* PSDs of both the 2016 observations also show the presence of a faint QPO-like structure at about 100 mHz (Fig. A7). We would like to point out that an additional sixth *NuSTAR* observation also exists during the rising phase, before the peak of the 2015 outburst. However, the PDS of this *NuSTAR* observation has a complex shape with four QPO-like features at 2, 9, 57, and 225 mHz frequencies. However, the analysis and interpretation of that observation are beyond the scope of this work.

We analysed the spectra from the two *XMM-Newton* and four *NuSTAR* observations. The *XMM-Newton*/PN spectra were re-binned with the HEASOFT tool FTGROUPPHA such that each spectral bin has a minimum number of counts equivalent to a signal-to-noise ratio (SNR) of ≥50 per bin. We tried to fit different continuum models to the 1–10 keV *XMM-Newton*/PN spectra of both observations and found that absorbed `powerlaw`, `compTT` and `NPEX` models could fit the continuum well. Residuals were left at around 6.7 and 2.2 keV

**Table 2.** The results of spectral fit performed on two observations of 4U 1626–67 having QPO. All observations were fitted with the composite spectral model `tbabs*(powerlaw+bbody+gaussian)`. The best-fitting model parameter values and their errors are given. The errors quoted on all parameters are their 90 per cent confidence ranges.

| | *XMM-Newton*/PN | | *NICER* |
|---|---|---|---|
| Obs. ID | 0 111 070 201 | 0152620101 | 62038001XX[$\ell$] |
| nH[†] | $0.05 \pm 0.01$ | $0.07 \pm 0.01$ | $0.07 \pm 0.03$ |
| PhoIndex ($\Gamma$) | $0.81 \pm 0.02$ | $0.80 \pm 0.01$ | $0.65 \pm 0.11$ |
| $N_{PL}$[‡] | $(8.1 \pm 0.2) \times 10^{-3}$ | $(6.8 \pm 0.1) \times 10^{-3}$ | $(5.1 \pm 0.6) \times 10^{-3}$ |
| $kT_{bbody}$ (keV) | $0.27 \pm 0.01$ | $0.24 \pm 0.01$ | $0.23 \pm 0.02$ |
| $N_{bbody}$[§] | $(1.2 \pm 0.1) \times 10^{-4}$ | $(1.10 \pm 0.04) \times 10^{-4}$ | $(7.8 \pm 2.3) \times 10^{-5}$ |
| $E_{Gauss}$ | $1.00 \pm 0.01$ | $1.01 \pm 0.01$ | $1.00 \pm 0.02$ |
| $\sigma_{Gauss}$ | $0.04 \pm 0.01$ | $0.02^{+0.01}_{-0.02}$ | $0.01$[★] |
| $N_{Gauss}$[¶] | $(3.9 \pm 0.5) \times 10^{-4}$ | $(2.1 \pm 0.2) \times 10^{-4}$ | $(1.2 \pm 0.3) \times 10^{-4}$ |
| Flux$_{2-20\,keV}$ ($10^{-10}$ erg s$^{-1}$ cm$^{-2}$) | $2.90 \pm 0.01$ | $2.31 \pm 0.01$ | $1.70 \pm 0.17$ to $6.05 \pm 0.17$ |
| $\chi^2$ (dof) | 1823 (1642) | 2153 (1896) | 74(94) to 122(95) |
| $\chi^2_{red}$ | 1.11 | 1.14 | 0.79 to 1.29 |

[★] Frozen.

[†] in units of $10^{22}$ atoms cm$^{-2}$.

[‡] Normalization in units of photons s$^{-1}$ cm$^{-2}$ keV$^{-1}$ at 1 keV.

[§] Normalization in units of $10^{37}$ ergs s$^{-1}$ kpc$^{-2}$.

[¶] Total photons s$^{-1}$ cm$^{-2}$ in the gaussian line.

[$\ell$] XX = 03, 04, 06, 11, 12, 15–17, 22, 32, 33, 35–42, 45–47, and 49. The quoted best-fitting parameter values are the error-weighted mean and standard error of the parameter estimates from individual observations. The ranges of variation of flux and fit-statistic are given. The best-fitting model on observations XX = 38 and 45 having relatively short exposure duration did not require a blackbody component.
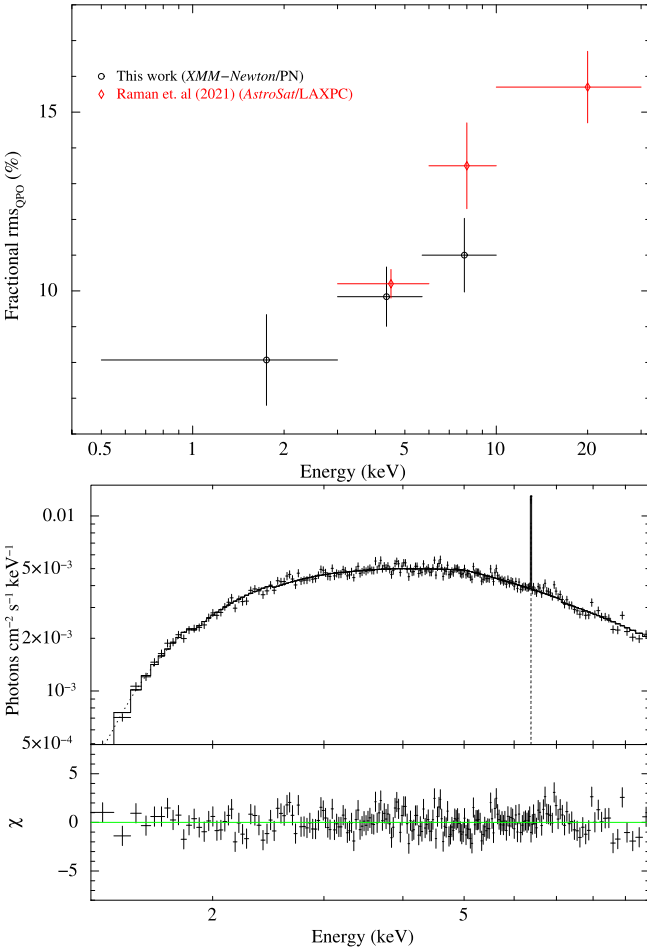


**Figure 3.** Top: The energy dependent variation of QPO fractional rms amplitude in IGR J19294 + 1816 from *XMM-Newton* (*this work*; black) and *Astrosat*/LAXPC (red; Raman et al. 2021). Bottom: The 0.5–10 keV unfolded *XMM-Newton*/PN spectrum and residuals to the best-fitting model `tbabs * (powerlaw * highecut + gaussian)`.

**Table 3.** The results of spectral fit performed on one observation of IGR J19294 + 1816 having QPO. The best-fitting model parameter values and their errors are given. The errors quoted on all the parameters are their 90 per cent confidence ranges.

| Obs. ID | 0841190101 |
|---|---|
| nH[†] | $3.62 \pm 0.17$ |
| PhoIndex ($\Gamma$) | $0.41 \pm 0.07$ |
| $N_{PL}$[‡] | $0.010 \pm 0.001$ |
| cutoffE (keV) | $4.96 \pm 0.30$ |
| foldE (keV) | $7.03 \pm 0.50$ |
| $E_{Gauss, Fe}$ | $6.39 \pm 0.01$ |
| $\sigma_{Gauss, Fe}$ | $0.01$[★] |
| $N_{Gauss, Fe}$[¶] | $(2.9 \pm 0.4) \times 10^{-4}$ |
| Flux$_{2-20\,keV}$ ($10^{-10}$ erg s$^{-1}$ cm$^{-2}$) | $4.04 \pm 0.02$ |
| $\chi^2$ (dof) | 679 (669) |
| $\chi^2_{red}$ | 1.02 |

[★] Frozen.

[†] in units of $10^{22}$ atoms cm$^{-2}$.

[‡] Normalization in units of photons s$^{-1}$ cm$^{-2}$ keV$^{-1}$ at 1 keV. [¶] Total photons s$^{-1}$ cm$^{-2}$ in the Gaussian line.

in both observations and we used two `Gaussians` centred at 6.7 and 2.2 keV to model them. The width of the 2.2 keV line was not constrained by the fit in both observations and therefore we froze it to 10 eV. We finally used the `NPEX` model as other continuum models left residuals around the iron fluorescence region. Soft-excess-like residuals were visible at the lowest energies only in OID 0 763 470 301, and we used a `bbody` with $kT \sim 0.1$ keV to model it. The finally used model for the two *XMM-Newton* observations are `tbabs*(NPEX + gaussian_1 + gaussian_2 + bbody)`, and `tbabs*(NPEX + gaussian_1 + gaussian_2)`.

The *NuSTAR*/FPM spectra were re-binned with the same tool as per the optimal binning scheme developed by Kaastra & Bleeker (2016). We found that the continuum of the 3–55 keV *NuSTAR* spectra could be well modelled with an absorbed `powerlaw` with a high-energy cutoff (`highecut`, `newhcut`) or `compTT`. We used the simplest high-energy-cutoff model `highecut`. An additional
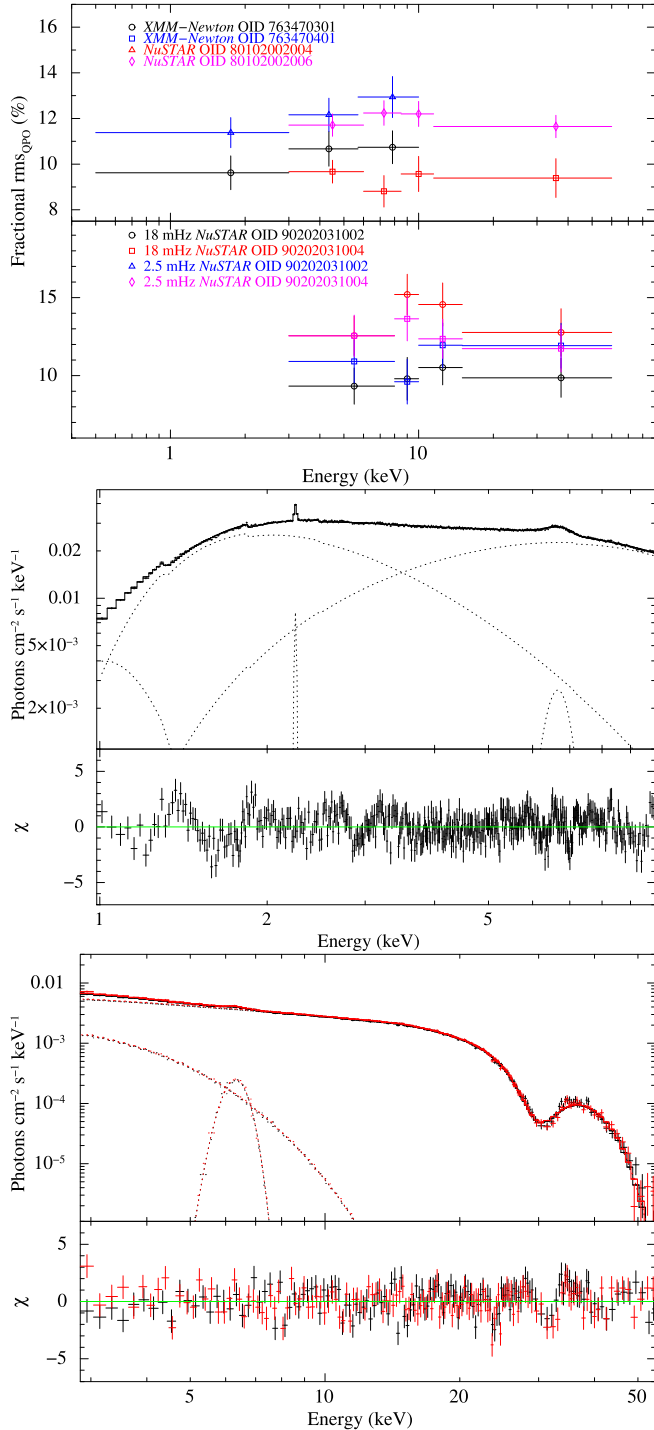
**Figure 4.** Top: The top and bottom panels show the energy dependence of the ~40 mHz, and ~2.5, ~18 mHz QPOs in V 0332+53. Middle: The 1–10 keV unfolded spectrum and residuals to the best-fitting spectral model `tbabs * (NPEX + gaussian + bbody)` on the *XMM-Newton* observation OID 0763470401. Bottom: The 3–55 keV unfolded spectrum and residuals to the best-fitting spectral model `tbabs * (powerlaw * mplcut + gaussian + bbody)` on the *NuSTAR* observation OID 90202031002.

`gabs` centred at the cutoff energy was included to flatten the kink at $E_{cut}$ (`mplcut`; Coburn et al. 2002). The absorption column density could not be constrained by the fit, so we froze it to the Galactic value of $0.7 \times 10^{22}$ atoms cm$^{-2}$. Significant residuals were left at ~30 keV (the fundamental CRSF; Vybornov, V. et al.

2018) and they could be modelled with a `gabs` or a `cyclabs` model, and we adopted `cyclabs` owing to its better fit-statistic. However, to flatten the residuals completely in 2015 observations, we added one more narrow `gabs` at ~30 keV. This could be due to poor modelling of the underlying continuum or a complex CRSF profile (Doroshenko et al. 2017). Residuals were also left at ~55 keV due to the harmonic CRSF (Vybornov, V. et al. 2018), which could be eliminated by the harmonic CRSF parameters of the `cyclabs`. Residuals were left at 6.4 keV (iron fluorescence), and we fitted it with a `Gaussian`. Soft-excess-like residuals were visible, and we modelled it with a `bbody` of $kT$ ~0.3 keV in 2015 observations and $kT$ ~1.0 keV in 2016 observations. The final used model for the 2015 and 2016 *NuSTAR* observations are `tbabs*(powerlaw*mplcut*cyclabs*gabs+bbody + gaussian)`, and `tbabs*(powerlaw*mplcut*cyclabs +bbody + gaussian)`, respectively. The best-fitting spectral model parameters are given in Table 4.

### 3.4 Cen X–3

Cen X–3 is a persistent 208 mHz XRP accreting matter from a massive O-type 20 $M_\odot$ supergiant companion star in a compact, nearly circular 2.2 d orbit (Suchy et al. 2008, and references therein). The accretion is expected to be partly from stellar wind and partly from the accretion disc due to the overall spin-up trend of the pulsar (Petterson 1978). Cen X–3 shows QPO at different frequencies ranging from 30 mHz (this work) to 90 mHz (Raichur & Paul 2008). Raichur & Paul (2008) and Liu et al. (2022) have shown that the QPO frequency or rms showed no dependence on the X-ray luminosity. Even though Raichur & Paul (2008) reported that the 40 mHz QPO rms does not show any energy dependence in the 1996–1998 *RXTE* observations, recently Liu et al. (2022) showed that the 40 mHz QPO rms decreases from 13 per cent at 2 keV to about 9 per cent at 17 keV in the 2020 *Insight-HXMT* observations. They further argued that the QPO frequency and rms have an orbital dependence and that the QPO photons show an overall soft lag.

We detected the presence of a QPO at around 30 mHz in one *XMM-Newton* observation that was conducted in the out-of-eclipse orbital phase. The PDS in 7.5–120 mHz range was modelled with the combination of a `powerlaw` for the band-limited noise and a `Lorentzian` at 30 mHz for the QPO (Fig. A8). The QPO rms shows a weak increasing trend with photon energy, increasing from about 5 per cent in 0.5–3 keV to about 6 per cent in 3–10 keV (Fig. 5).

The *XMM-Newton*/PN spectrum was re-binned such that each bin has counts equivalent to a minimum SNR of 50. We adopted the spectral model of the source used in Aftab, Paul & Kretschmar (2019). The spectrum was modelled with an absorbed `powerlaw` for the continuum, a `bbody` with kT~0.1 keV, and eleven `Gaussian` emission lines. The iron line emission region is complex, and it was modelled with a combination of two narrow `Gaussians` at 6.44 and 6.65 keV, and a broad `Gaussian` at 6.65 keV. The complex iron region is possibly due to three distinct iron lines at 6.4, 6.7, and 7 keV (Naik & Paul 2012). The finally used best-fitting spectral model is `tbabs*(powerlaw+bbody + 11×Gaussians)` (Fig. 5). The best-fitting spectral model parameters are given in Table 5.

### 3.5 XTE J1858 + 034

XTE J1858 + 034 is a transient XRP spinning at 4.5 mHz. The binary is thought to be a Be-type HMXB due to its transient nature (Takeshima et al. 1998) and nature of the optical companion (Reig et al. 2005). However, a recent study by Tsygankov et al. (2021)

**Table 4.** The results of spectral fit performed on four observations of V 0332+53 having a QPO. The best-fitting model parameter values and their errors are given. The errors quoted on all the parameters are their 90 per cent confidence ranges.

| | XMM-Newton/PN | | NuSTAR$^{\top}$ | | | |
|---|---|---|---|---|---|---|
| Obs. ID | 0763470401 | 0763470301 | 80102002004 | 80102002006 | 90202031002 | 90202031004 |
| Continuum | tbabs*NPEX | tbabs*NPEX | tbabs*powerlaw*mpl cut | tbabs*powerlaw*mpl cut | tbabs*powerlaw*mpl cut | tbabs*powerlaw*mpl cut |
| Energy range | 1–10 keV | 1–10 keV | 3–55 keV | 3–55 keV | 3–55 keV | 3–55 keV |
| nH$^{\dagger}$ | $2.19 \pm 0.07$ | $2.17 \pm 0.06$ | $2.07^{+1.04}_{-0.90}$ | $0.43^{+0.94}_{-0.44}$ | $0.7^*$ | $0.7^*$ |
| PhoIndex ($\Gamma$) | $1.06 \pm 0.05$ | $1.04 \pm 0.05$ | $0.53 \pm 0.02$ | $0.49 \pm 0.02$ | $0.57^{+0.03}_{-0.04}$ | $0.57^{+0.04}_{-0.02}$ |
| $N_{CPL/PL} - 1^{\ddagger}$ | $0.15 \pm 0.01$ | $0.18 \pm 0.01$ | $0.18 \pm 0.01$ | $0.106^{+0.006}_{-0.003}$ | $0.011 \pm 0.001$ | $0.008 \pm 0.001$ |
| $E_{cut}$ | $3.41 \pm 0.03$ | $3.27 \pm 0.03$ | $10.90^{+0.18}_{-0.21}$ | $11.95^{+0.18}_{-0.21}$ | $15.17^{+0.84}_{-0.39}$ | $16.31^{+0.39}_{-0.36}$ |
| $E_{fold}$ | — | — | $17.23^{+1.65}_{-1.32}$ | $16.79^{+0.96}_{-0.97}$ | $26.21^{+4.30}_{-9.24}$ | $16.58^{+4.34}_{-2.88}$ |
| $N^{\dagger}_{CPL/PL-2}$ | $(2.93 \pm 0.08) \times 10^{-3}$ | $(4.00 \pm 0.10) \times 10^{-3}$ | — | — | — | — |
| $E_{Gauss, Fe}$ | $6.64 \pm 0.02$ | $6.66 \pm 0.02$ | $6.44 \pm 0.02$ | $6.46 \pm 0.03$ | $6.3 \pm 0.10$ | $6.37 \pm 0.07$ |
| $\sigma_{Gauss, Fe}$ | $0.25 \pm 0.02$ | $0.35^{+0.03}_{-0.02}$ | $0.34 \pm 0.04$ | $0.38 \pm 0.04$ | $0.36^{+0.17}_{-0.15}$ | $0.15^{+0.13}_{-0.15}$ |
| $N^{\P}_{Gauss,Fe}$ | $(1.35 \pm 0.08) \times 10^{-3}$ | $(2.34 \pm 0.15) \times 10^{-3}$ | $0.005 \pm 0.001$ | $(3.77 \pm 0.44) \times 10^{-3}$ | $(2.25) \times 10^{-4}$ | $(1.23^{+0.04}_{-0.37}) \times 10^{-4}$ |
| $E_{Gauss, 2}$ | $2.25 \pm 0.01$ | $2.25 \pm 0.01$ | — | — | — | — |
| $\sigma_{Gauss, 2}$ | $0.01^*$ | $0.01^*$ | — | — | — | — |
| $N^{\P}_{Gauss,2}$ | $(2.65 \pm 0.52) \times 10^{-4}$ | $(3.53 \pm 0.60) \times 10^{-4}$ | — | — | — | — |
| $kT_{bbody}$ (keV) | — | $0.089 \pm 0.003$ | $0.33^{+0.04}_{-0.06}$ | $0.34 \pm 0.10$ | $0.88^{+0.09}_{-0.07}$ | $0.97^{+0.08}_{-0.09}$ |
| $N^{\S}_{bbody}$ | — | $0.10 \pm 0.02$ | $0.03^{+0.05}_{-0.01}$ | $0.01 \pm 0.01$ | $(3.38^{+0.69}_{-0.57}) \times 10^{-4}$ | $(3.17^{+0.68}_{-0.58}) \times 10^{-4}$ |
| Flux$_{2-20\,keV}$ ($10^{-10}$ erg s$^{-1}$ cm$^{-2}$) | $29.05 \pm 0.02$ | $35.01 \pm 0.03$ | $124.80 \pm 0.08$ | $83.07 \pm 0.07$ | $7.51 \pm 0.02$ | $6.08 \pm 0.01$ |
| const | — | — | $0.980 \pm 0.001$ | $0.978 \pm 0.002$ | $1.025 \pm 0.004$ | $1.04 \pm 0.01$ |
| $\chi^2$ (dof) | 1502.83 (1256) | 1600.27 (1417) | 538.75 (401) | 537.59 (377) | 418.66 (331) | 364.12 (323) |
| $\chi^2_{red}$ | 1.20 | 1.13 | 1.34 | 1.43 | 1.27 | 1.13 |

$^*$ Frozen.

$^{\dagger}$ in units of $10^{22}$ atoms cm$^{-2}$.

$^{\ddagger}$ Normalization in units of photons s$^{-1}$ cm$^{-2}$ keV$^{-1}$ at 1 keV.

$^{\P}$ Total photons s$^{-1}$ cm$^{-2}$ in the gaussian line.

$^{\S}$ Normalization in units of $10^{37}$ ergs s$^{-1}$ kpc$^{-2}$.

$^{\top}$ A CRSF at 29 keV and its harmonic is modelled with cyclabs and gabs models, the parameters of which are not given in this table.
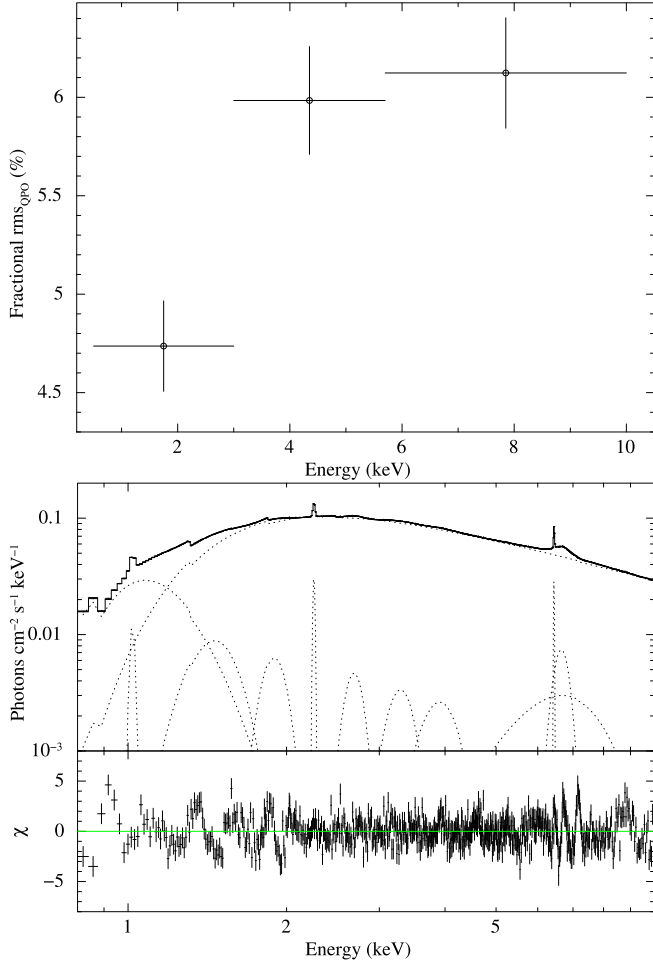
**Figure 5.** Top: The energy dependence of QPO rms in Cen X–3 from *XMM-Newton*. Bottom: The 0.8–10 keV unfolded *XMM-Newton*/PN spectrum and residuals to the best-fitting model `tbabs * (cutoffpl + bbody + (10)gaussians)`.

proposed that the system could be a Symbiotic binary hosting a K/M type stellar companion. QPO was first reported in the source from an *RXTE*/PCA observation by Paul & Rao (1998) at 110 mHz. In subsequent outbursts, Mukherjee et al. (2006) found the centroid frequency of the QPO being variable from 140 to 185 mHz and that rms amplitude of QPO has a strong correlation with photon energy. QPO was again reported in the *NuSTAR* observation at 196 mHz by Mandal & Pal (2021) during an outburst of the source in 2019.

We generated the energy-dependent variation of fractional rms amplitude of the QPO detected at 196 mHz (Fig. A9), the same one reported by Mandal & Pal (2021). The QPO is detected only till 25 keV. The *NuSTAR* PDS in 5–1000 mHz was fitted with the combination of a `powerlaw` for the band-limited noise and a `Lorentzian` for the QPO (Fig. A4). The QPO rms increases from about 5 per cent in 3–8 keV to about 11 per cent in 15–25 keV (Fig. 6).

We adopted the spectral model of the source used by Malacaria et al. (2021). The 5–55 keV *NuSTAR* spectrum could be fitted with a `compTT` continuum, modified by the CRSF at 50 keV with a `gabs`, and an iron emission line at 6.4 keV with a `gaussian` (Fig. 6). The best-fitting spectral model parameters are given in Table 6.

**Table 5.** The results of spectral fit performed on the *XMM-Newton* observation of Cen X–3 having a QPO. The best-fit model parameter values and their errors are given. The errors quoted on all the parameters are their 90 per cent confidence ranges.

| Obs. ID | 040550201 |
|---|---|
| Continuum – – | |
| $nH_1$ | $2.43 \pm 0.03$ |
| PhoIndex ($\Gamma$) | $1.175 \pm 0.004$ |
| $N_{PL}^{\ddagger}$ | $0.444 \pm 0.003$ |
| $kT_{bbody}$ | $0.096 \pm 0.001$ |
| $N_{bbody}^{\S}$ | $0.64_{-0.08}^{+0.09}$ |
| Iron emission lines complex – – | |
| $E_{Gauss, 1}$ | $6.44_{-0.01}^{+0.01}$ |
| $\sigma_{Gauss, 1}$ | $0.01^{\star}$ |
| $N_{Gauss,1}^{\P}$ | $9.74_{-0.64}^{+0.62} \times 10^{-4}$ |
| $E_{Gauss, 2}$ | $6.65 \pm 0.01$ |
| $\sigma_{Gauss, 2}$ | $0.22_{-0.01}^{+0.01}$ |
| $N_{Gauss,2}^{\P}$ | $(4.16 \pm 0.02) \times 10^{-3}$ |
| $E_{Gauss, 3}$ | $6.65 \pm 0.01$ |
| $\sigma_{Gauss, 3}$ | $1.21_{-0.08}^{+0.10}$ |
| $N_{Gauss,3}^{\P}$ | $0.009 \pm 0.001$ |
| Other emission lines – – | |
| $E_{Gauss, 4}$ | $1.018 \pm 0.004$ |
| $\sigma_{Gauss, 4}$ | $0.019 \pm 0.002$ |
| $N_{Gauss,4}^{\P}$ | $0.22_{-0.01}^{+0.01}$ |
| $E_{Gauss, 5}$ | $1.39_{-0.01}^{+0.01}$ |
| $\sigma_{Gauss, 5}$ | $0.16_{-0.01}^{+0.01}$ |
| $N_{Gauss,5}^{\P}$ | $0.019 \pm 0.003$ |
| $E_{Gauss, 6}$ | $1.89_{-0.01}^{+0.01}$ |
| $\sigma_{Gauss, 6}$ | $0.10_{-0.01}^{+0.01}$ |
| $N_{Gauss,6}^{\P}$ | $3.43_{-0.61}^{+0.80} \times 10^{-3}$ |
| $E_{Gauss, 7}$ | $2.254 \pm 0.003$ |
| $\sigma_{Gauss, 7}$ | $0.1^{\star}$ |
| $N_{Gauss,7}^{\P}$ | $1.38_{-0.13}^{+0.15} \times 10^{-3}$ |
| $E_{Gauss, 8}$ | $2.68_{-0.01}^{+0.01}$ |
| $\sigma_{Gauss, 8}$ | $0.10_{-0.01}^{+0.01}$ |
| $N_{Gauss,8}^{\P}$ | $1.68_{-0.19}^{+0.25} \times 10^{-3}$ |
| $E_{Gauss, 9}$ | $3.29_{-0.02}^{+0.02}$ |
| $\sigma_{Gauss, 9}$ | $0.18_{-0.02}^{+0.02}$ |
| $N_{Gauss,9}^{\P}$ | $0.16_{-0.01}^{+0.01}$ |
| $E_{Gauss, 10}$ | $3.90_{-0.04}^{+0.03}$ |
| $\sigma_{Gauss, 10}$ | $0.30_{-0.04}^{+0.05}$ |
| $N_{Gauss,10}^{\P}$ | $(2.20 \pm 0.03) \times 10^{-3}$ |
| $Flux_{2-20\,keV}$ ($10^{-10}$ erg s$^{-1}$ cm$^{-2}$) | $67.12 \pm 0.02$ |
| $\chi^2$ (dof) | 2496.02/1813 |
| $\chi_{red}^2$ | 1.38 |

$\ddagger$ Normalization in units of photons s$^{-1}$ cm$^{-2}$ keV$^{-1}$ at 1 keV.
$\S$ Normalization in units of $10^{37}$ ergs s$^{-1}$ kpc$^{-2}$.
$\P$ Total photons s$^{-1}$ cm$^{-2}$ in the gaussian line.

## 4 DISCUSSIONS

Our search for QPOs in the archival *XMM-Newton* and *NuSTAR* observations resulted in the detection of QPO in eleven observations of five sources viz., 4U 1626–67 (*XMM-Newton*; Fig. A1), IGR J19294 + 1816 (*XMM-Newton*; Fig. A4), V 0332+53 (*XMM-Newton*, *NuSTAR*; Figs A5, A6, and A7), Cen X–3 (*XMM-Newton*; Fig. A8), and XTE J1858 + 034 (*NuSTAR*; Fig. A9). A summary of the QPO parameters in different energy bands of each observation is given in Table 7. The highest QPO rms is observed in the 48 mHz QPO in 4U 1626 – 67 ($\gtrsim 15$ per cent), followed by V 0332+53
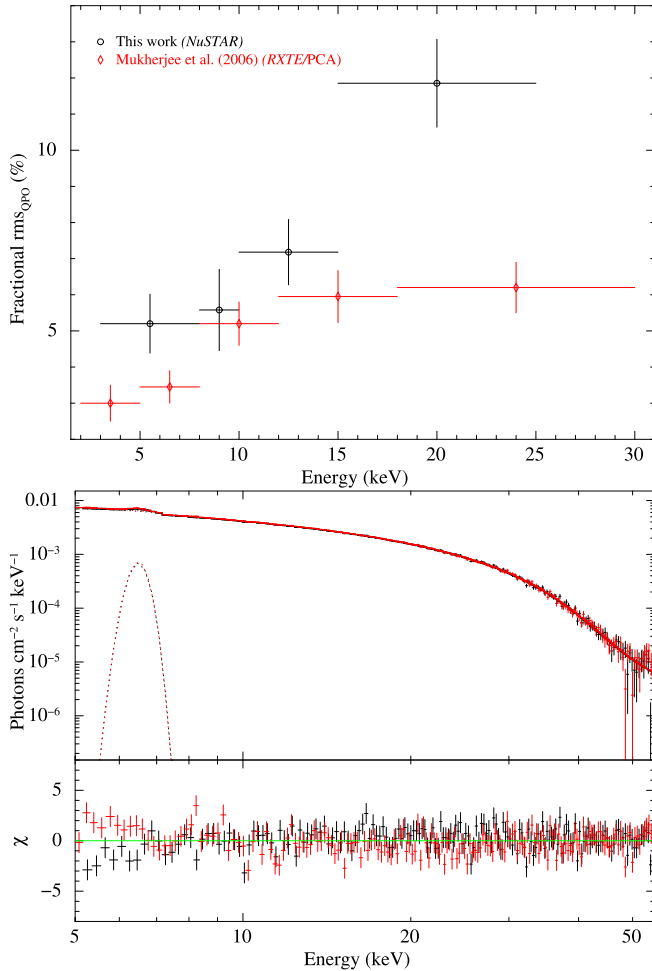
**Figure 6.** Top: XTE J1858 + 034 QPO rms energy dependence from *NuSTAR* (black) and *RXTE*/PCA (red; Mukherjee [2006]). Bottom: The 3–60 keV unfolded spectrum and residuals to the best-fitting spectral model (`tbabs * (compTT * gabs + gaussian)`) on the *NuSTAR* observation with OID 90501348002.

**Table 6.** The results of spectral fit performed on the *NuSTAR* observation of XTE J1858 + 034 having QPO. The best-fitting model parameter values and their errors are given. The errors quoted on all the parameters are their 90 per cent confidence ranges.

| Obs. ID | 90501348002 |
|---|---|
| $nH^{\dagger}$ | $8.49 \pm 2.29$ |
| $kT_0$ | $0.98 \pm 0.05$ |
| $kT_e$ | $5.80 \pm 0.15$ |
| $\tau$ | $6.60 \pm 0.30$ |
| $N_{norm}$ | $0.020 \pm 0.001$ |
| $E_{CRSF}$ | $51.09 \pm 2.06$ |
| $\sigma_{CRSF}$ | $10.74 \pm 1.81$ |
| $\tau_{CRSF}$ | $0.25 \pm 0.06$ |
| $E_{Gauss, Fe}$ | $6.48 \pm 0.03$ |
| $\sigma_{Gauss, Fe}$ | $0.25 \pm 0.05$ |
| $N^{\P}_{Gauss, Fe}$ | $(5 \pm 1) \times 10^{-4}$ |
| $Flux_{2-20 keV}$ ($10^{-10}$ erg s$^{-1}$ cm$^{-2}$) | $10.35 \pm 0.02$ |
| const. | $1.018 \pm 0.003$ |
| $\chi^2$(dof) | 411.50/337 |
| $\chi^2_{red}$ | 1.22 |

$\dagger$ in units of $10^{22}$ atoms cm$^{-2}$.

$\P$ Total photons s$^{-1}$ cm$^{-2}$ in the gaussian line.

($\gtrsim 10$ per cent). The QPO rms is $< 10$ per cent in all the other cases. In Cen X–3 and XTE J1858 + 034, the QPO rms is low at $\lesssim 6$ per cent below 10 keV. We discuss the observed QPO characteristics in various contexts below.

### 4.1 Transient nature of QPOs

The transient nature of QPOs in XRPs is evident from detection and non-detection in different observations of the same source (Tables 1 and B1). Some observations could however be made regarding the appearance/disappearance of QPOs in certain observations of a source analysed in this work.

In the four observations of 4U 1626 − 67 analysed in this work, QPO has been detected in three observations and not detected in one observation. 4U 1626 − 67 was in the spin-down torque-state of the pulsar between 1990 and 2008, and since 2023 (Sharma, Jain & Paul [2023b]). The three observations (Table 1) having the 48 mHz QPO were taken when the pulsar was in the spin-down state. The source was observed in the spin-up torque state of the pulsar in the observation without QPO (*XMM-Newton* OID 0 764 860 101 in 2015). The appearance of the 48 mHz QPO only during the spin-down state of the pulsar has been previously reported by Jain et al. [2010] and Sharma et al. [2023b]. 4U 1626 − 67 is the only XRP where the QPO is persistently present during a specific torque state of the pulsar.

Among the three observations of IGR J19294 + 1816, QPO was only detected in one observation. The *XMM-Newton* observation in which the QPO at ~30 mHz is present, was taken at the luminosity rising phase during a Type-I outburst of Be-XRP in October 2019. Raman et al. [2021] has reported the presence of QPO at around the same frequency during the luminosity decline phase of the same outburst with *Astrosat*/LAXPC. QPO was not observed in the two *NuSTAR* observations, of which OID 90 401 306 002 was done when the source was in a low-luminosity state in March 2018 and OID 90 401 306 004 was taken immediately following a Type-I outburst in the same month (Tsygankov et al. [2019b]).

In the three observations of Cen X–3, a QPO at 30 mHz is present in only one observation (Table 1) and it covers the out-of-eclipse orbital phase of the source (Aftab et al. [2019]), and not present in the two eclipse-egress orbital phase observations (*XMM-Newton* OID 0 111 010 101 that covers orbital phase 0.00 − 0.37; Sanjurjo-Ferrín et al. [2021], and *NuSTAR* OID 30 101 055 002 that covers orbital phase 0.20 − 0.41; Tamba et al. [2023]). 30 mHz is the lowest QPO frequency reported in Cen X–3. Raichur & Paul [2008] had found QPO frequency clustering around 40 and 90 mHz from *RXTE*/PCA observations during 1996–1998. Liu et al. [2022] observed that the QPO frequency varies as a function of the orbital phase from about 33 mHz in the eclipse egress phase (0.1–0.3) to about 40 mHz in the pre-ingress phase (0.8) from *Insight-HXMT* observations in 2022.

Among the nine observations of V 0332+53, QPO is present in six observations. Seven out of the nine observations were taken during a Type-II outburst of the source in 2015. This includes two *XMM-Newton* and five *NuSTAR* observations. Two quasi-simultaneous *NuSTAR* and *XMM-Newton* observations taken mid-way during the decline of Type-II outburst (Doroshenko et al. [2017]; Vybornov, V. et al. [2018]) have the presence of QPO at 40 mHz. However, two other *NuSTAR* observations taken towards the end of the decline of the 2015 outburst (Doroshenko et al. [2017]; Vybornov, V. et al. [2018]) does not show QPO. The two *NuSTAR* observations during a Type-I outburst in 2016 have the presence twin-QPOs at ~2.5 and ~18 mHz (See discussion in Section 4.3). The *XMM-Newton* observation taken during the quiescent state of the source in 2008 (Elshamouty,

**Table 7.** Summary of the QPO fits. The continuum is fitted with either or a combination of *powerlaw*, *lorentzian* and the QPO is fitted with a *Lorentzian*. The centre and width of the *Lorentzian* are considered the centroid and width of the QPO, respectively. Errors assigned to the centroid and width of the QPO are their 90 per cent confidence intervals, while error assigned to the rms powers are their 68 per cent confidence intervals.

| Source | Obs. ID | Energy range (keV) | Avg. count rate[7] (cts s$^{-1}$) | $\nu_{QPO}$ (mHz) | width$_{QPO}$ (mHz) | Power$_{rms}$ (per cent) | $Q$-factor |
|---|---|---|---|---|---|---|---|
| 4U 1626–67 | 0 111 070 201 | 0.5–1.0 | 5.53 ± 0.03 | 48 ± 1 | 12 ± 3 | 18.34 ± 1.06 | 4.0 |
| | | 1.0–3.0 | 13.35 ± 0.04 | 49 ± 1 | 13 ± 3 | 20.74 ± 0.96 | 3.8 |
| | | 3.0–5.7 | 6.19 ± 0.03 | 49 ± 2 | 14 ± 7 | 15.69 ± 1.41 | 3.5 |
| | | 5.7–10.0 | 4.08 ± 0.02 | 49 ± 1 | 11 ± 4 | 18.54 ± 1.44 | 4.5 |
| | 0 152 620 101 | 0.5–1.0 | 4.63 ± 0.01 | 48 ± 1 | 11 ± 2 | 17.65 ± 0.51 | 4.3 |
| | | 1.0–3.0 | 10.96 ± 0.02 | 48 ± 1 | 11 ± 1 | 20.61 ± 0.48 | 4.2 |
| | | 3.0–5.7 | 5.24 ± 0.01 | 47 ± 1 | 11 ± 2 | 17.11 ± 0.60 | 4.3 |
| | | 5.7–10.0 | 3.53 ± 0.10 | 48 ± 1 | 10 ± 2 | 16.86 ± 0.73 | 4.5 |
| | P10101 | 2.02–6.70 | 61.23 ± 0.02 | 48.2 ± 0.3 | 11 ± 1 | 16.83 ± 0.44 | 4.4 |
| | | 6.7–8.5 | 31.75 ± 0.02 | 48.3 ± 0.3 | 10 ± 1 | 16.65 ± 0.39 | 4.8 |
| | | 8.5–11.1 | 35.33 ± 0.02 | 48.4 ± 0.3 | 11 ± 1 | 17.45 ± 0.35 | 4.4 |
| | | 11.1–13.0 | 19.40 ± 0.01 | 48.2 ± 0.3 | 10 ± 1 | 18.23 ± 0.41 | 4.8 |
| | | 13.0–15.4 | 16.31 ± 0.01 | 48.3 ± 0.3 | 11 ± 1 | 19.83 ± 0.36 | 4.4 |
| | | 15.4–20.2 | 19.67 ± 0.01 | 48.4 ± 0.3 | 11 ± 1 | 21.45 ± 0.35 | 4.4 |
| | | 20.2–60.0 | 11.38 ± 0.02 | 48.7 ± 0.5 | 9 ± 1 | 28.32 ± 0.98 | 5.4 |
| | 62038001 | 0.5–0.9 | 5.89 ± 0.03 | 47 ± 1 | 12 ± 3 | 13.59 ± 0.69 | 3.9 |
| | | 0.9–1.3 | 5.74 ± 0.03 | 47 ± 1 | 12 ± 3 | 17.26 ± 0.69 | 3.6 |
| | | 1.3–1.9 | 5.91 ± 0.03 | 48 ± 1 | 15 ± 3 | 19.59 ± 0.83 | 3.2 |
| | | 1.9–3.5 | 6.44 ± 0.03 | 49 ± 2 | 17 ± 5 | 19.10 ± 1.10 | 2.9 |
| IGR J19294 + 1816 | 0 841 190 101 | 0.5–3 | 4.38 ± 0.02 | 29 ± 1 | 8 ± 5 | 8.07 ± 1.27 | 7.8 |
| | | 3.0–5.7 | 8.95 ± 0.02 | 31 ± 1 | 9 ± 3 | 9.84 ± 0.83 | 3.6 |
| | | 5.7–10.0 | 7.70 ± 0.03 | 31 ± 1 | 10 ± 5 | 11.00 ± 1.03 | 3.0 |
| V 0332+53 | 0 763 470 301 | 0.5–3 | 123.77 ± 0.11 | 38 ± 3 | 38 ± 8 | 9.62 ± 0.74 | 1.0 |
| | | 3.0–5.7 | 153.56 ± 0.18 | 39 ± 2 | 33 ± 7 | 10.67 ± 0.76 | 1.2 |
| | | 5.7–10.0 | 147.28 ± 0.12 | 38 ± 2 | 38 ± 7 | 10.74 ± 0.72 | 1.8 |
| | 80102002004 | 3.0–6.0 | 123.09 ± 0.13 | 40 ± 1 | 37 ± 8 | 9.67 ± 0.50 | 1.1 |
| | | 6.0–8.5 | 139.10 ± 0.13 | 38 ± 2 | 24 ± 5 | 8.81 ± 0.69 | 1.6 |
| | | 8.5–11.5 | 147.92 ± 0.13 | 39 ± 2 | 32 ± 8 | 9.57 ± 0.77 | 1.2 |
| | | 11.5–60.0 | 163.67 ± 0.14 | 40 ± 2 | 36 ± 10 | 9.39 ± 0.85 | 1.1 |
| | 0 763 470 401 | 0.5–3 | 84.54 ± 0.07 | 41 ± 1 | 22 ± 6 | 11.38 ± 0.66 | 1.9 |
| | | 3.0–5.7 | 100.66 ± 0.13 | 42 ± 1 | 21 ± 5 | 12.16 ± 0.73 | 2.0 |
| | | 5.7–10.0 | 95.23 ± 0.07 | 42 ± 1 | 22 ± 5 | 12.94 ± 0.90 | 2.0 |
| | 80102002006 | 3.0–6.0 | 79.40 ± 0.08 | 41 ± 1 | 21 ± 4 | 11.71 ± 0.49 | 2.0 |
| | | 6.0–8.5 | 89.54 ± 0.09 | 41 ± 1 | 20 ± 4 | 12.24 ± 0.54 | 2.1 |
| | | 8.5–11.5 | 99.43 ± 0.09 | 41 ± 1 | 19 ± 3 | 12.20 ± 0.55 | 2.1 |
| | | 11.5–60.0 | 112.81 ± 0.09 | 41 ± 1 | 20 ± 3 | 11.65 ± 0.49 | 2.1 |
| | 90202031002 | 3–8 | 14.69 ± 0.03 | 17.1 ± 0.4 | 2.7 ± 1.2 | 9.33 ± 1.16 | 6.3 |
| | | 8–10 | 6.00 ± 0.02 | 18.3 ± 0.7 | 3.3 ± 1.2 | 9.80 ± 1.37 | 5.5 |
| | | 10–15 | 9.15 ± 0.03 | 17.4 ± 0.3 | 2.0 ± 0.9 | 10.52 ± 1.11 | 8.7 |
| | | 15–60 | 6.29 ± 0.02 | 18.0 ± 0.5 | 2.8 ± 1.1 | 9.86 ± 1.25 | 6.4 |
| | | 3–8 | 14.69 ± 0.03 | 2.48 ± 0.05 | 0.27 ± 0.13 | 10.91 ± 1.38 | 9.2 |
| | | 8–10 | 6.00 ± 0.02 | 2.51 ± 0.05 | 0.11 ± 0.11 | 9.61 ± 1.43 | ≳11.4 |
| | | 10–15 | 9.15 ± 0.03 | 2.49 ± 0.05 | 0.23 ± 0.11 | 11.95 ± 1.43 | 10.8 |
| | | 15–60 | 6.29 ± 0.02 | 2.49 ± 0.05 | 0.29 ± 0.13 | 11.92 ± 1.44 | 8.6 |
| | 90202031004 | 3–8 | 12.05 ± 0.03 | 17.8 ± 0.9 | 4.4 ± 1.9 | 12.56 ± 1.26 | 4.1 |
| | | 8–10 | 4.88 ± 0.02 | 17.5 ± 0.8 | 4.9 ± 1.8 | 15.20 ± 1.30 | 3.6 |
| | | 10–15 | 7.46 ± 0.02 | 17.8 ± 0.8 | 5.5 ± 2.4 | 14.56 ± 1.38 | 3.2 |
| | | 15–60 | 5.14 ± 0.02 | 18.6 ± 1.2 | 4.7 ± 2.2 | 12.77 ± 1.52 | 4.0 |
| | | 3–8 | 12.05 ± 0.03 | 2.33 ± 0.08 | 0.36 ± 0.26 | 12.55 ± 1.33 | 6.5 |
| | | 8–10 | 4.88 ± 0.02 | 2.33 ± 0.08 | 0.40 ± 0.27 | 13.64 ± 1.41 | 5.8 |
| | | 10–15 | 7.46 ± 0.02 | 2.35 ± 0.05 | 0.18 ± 0.15 | 12.36 ± 1.26 | ≳10.2 |
| | | 15–60 | 5.14 ± 0.02 | 2.30 ± 0.12 | 0.40 ± 0.36 | 11.73 ± 1.49 | 5.8 |
| Cen X–3 | 040550201 | 0.5–3 | 187.88 ± 0.06 | 30 ± 1 | 26 ± 4 | 4.74 ± 0.16 | 1.2 |
| | | 3.0–5.7 | 186.94 ± 0.06 | 31 ± 1 | 23 ± 4 | 5.98 ± 0.19 | 1.4 |
| | | 5.7–10.0 | 118.63 ± 10.05 | 30 ± 1 | 23 ± 3 | 6.12 ± 0.20 | 1.3 |
| XTE J1858 + 034 | 90501348002 | 3–8 | 23.03 ± 0.03 | 178 ± 9 | 70 ± 30 | 5.20 ± 0.69 | 2.5 |
| | | 8–10 | 9.08 ± 0.02 | 185 ± 8 | 37 ± 22 | 6.02 ± 0.87 | 5.0 |
| | | 10–15 | 12.45 ± 0.02 | 183 ± 7 | 56 ± 20 | 7.07 ± 0.69 | 3.3 |
| | | 15–25 | 3.69 ± 0.01 | 186 ± 7 | 84 ± 27 | 11.73 ± 1.03 | 2.2 |

[7]Across all PCUs (*RXTE*) or FPMs (*NuSTAR*).

Heinke & Chouinard 2016; Tsygankov et al. 2017) does not have a QPO.

QPOs in Be-XRPs are generally associated with the formation of accretion discs during the outbursts (Reig & Nespoli 2013). In the two Be-XRPs analysed in this work (IGR J19294+1816 and V 0332+53), QPOs were detected in all the observations during high-luminosity phases of the Type-II outbursts and were detected in some Type-I outbursts while not in some other Type-I outbursts. However, no QPOs were detected in the observations that were carried out during their low-luminosity states. The presence of QPO only during the high-luminosity phases of the Type-II outbursts in Be-XRPs have been previously reported (Malacaria et al. 2024, and references therein).

### 4.2 Energy-dependence of QPOs

The energy spectra of all five sources had a smooth continuum shape absorbed by ISM at low energies, with atomic emission lines mainly of iron. Cen X−3, which has a companion that releases strong stellar wind had the presence of multiple emission lines. CRSF was present in all of them having *NuSTAR* observations. A soft excess was present in 4U 1626 − 67, Cen X−3, and V 0332+53 (Section 4.4).

The overall shape of the broad-band noise in PDS does not vary with energy in all the sources (Appendix A). However, the strengths of QPO and the pulsations vary with energy. We do not notice any strong trends in the QPO parameters (centre, width, $Q$-factor) except the fractional rms amplitude, as a function of energy in any of the sources (Table 7). There is also no secular trend in the QPO rms versus energy exhibited by all the sources. A correlation of fractional rms amplitude with energy is seen in 4U 1626 − 67 in 5–60 keV, IGR J19294+1816 in 0.5–30 keV, Cen X−3 in 0.5–10 keV, and XTE J1858+034 in 2–30 keV. No variation of fractional rms amplitude with energy is visible in V 0332+53. However, differences are noticed in the energy dependence of fractional rms between different observations (having the same QPO frequency) of the same source.

In XTE J1858 + 034, the fractional rms amplitude of the QPO during the November 2019 outburst (*this work*) is overall higher than during the outburst in May 2004 with *RXTE* observations (Mukherjee et al. 2006). The X-ray flux is similar ($\sim 10^{-9}$ ergs s$^{-1}$ cm$^{-2}$) for the two observations. The authors also observed that the QPO frequency changes from 150 to 180 mHz while the X-ray flux varies from $2.5 − 5.5 \times 10^{-9}$ ergs s$^{-1}$ cm$^{-2}$. The highest 180 mHz QPO frequency was observed at a flux of about $4 \times 10^{-9}$ ergs s$^{-1}$ cm$^{-2}$. In the *NuSTAR* observation we analysed, the QPO frequency is slightly higher than 180 mHz and the flux is about $1.4 \times 10^{-9}$ ergs s$^{-1}$ cm$^{-2}$. Even though a correlation of rms amplitude with energy is seen in both the outbursts, the trend is seen to deviate above 10 keV, where it saturates for the 2004 observations while the correlation continues in the 2019 observation. The absence of QPO above 30 keV is in agreement with Mukherjee et al. (2006).

In Cen X−3, the rms amplitude of 30 mHz QPO shows a correlation with energy as opposed to no correlation of the 40 mHz QPO in Raichur & Paul (2008) and a clear anticorrelation of the 30–40 mHz QPO seen in Liu et al. (2022). While Raichur & Paul (2008) reported the presence of QPO till 35 keV, Liu et al. (2022) observed no QPO above 20 keV.

The overall energy dependence of the rms amplitude of the 30 mHz QPO in IGR J19294 + 1816 during the onset of Type-I outburst in 2019 from this work is in agreement with Raman et al. (2021) during the decline of the same outburst.

Neither the twin-QPOs at 2.5 and 18 mHz in 2016 (0.5–60 keV) nor the QPO at 40 mHz in 2015 (3–60 keV) detected in V 0332+53 exhibit any energy dependence. This is different from the previous reports of Qu et al. (2005) where the rms of the twin QPOs at 50 mHz and 220 mHz detected during the 2015 Type-II outburst drops beyond 10 keV.

The 48 mHz QPO in 4U 1626 − 67 preserves the value of fractional rms amplitude and the correlation of QPO rms with energy across several observations spanning over two decades. During this time, the source has also exhibited multiple torque-state switches (Sharma et al. 2023b). A peculiarity of 4U 1626 − 67 is that it is the only Roche lobe overflow (RLO) LMXB in the list (Table 1), in which the accretion only proceeds via an accretion disc. Even though accretion in the compact HMXB Cen X−3 is also partially driven by RLO, there is also a significant contribution expected from the strong stellar wind. Cen X−3 in the long-term has shown a variety of QPO frequencies varying from 30 to 90 mHz and the energy trend of these QPOs are also different (Raichur & Paul 2008; Liu et al. 2022, and this work). It is also worth noting that the 48 mHz QPO in 4U 1626 − 67 has exhibited the highest rms amongst the list ($\gtrsim 15$ per cent), while Cen X−3 has the lowest ($\lesssim 6$ per cent).

### 4.3 Twin QPOs in V 0332+53

The QPOs we detected in V 0332+53 at 2.5 mHz, 18 mHz (2016 Type-I outburst) and 40 mHz (2015 Type-II outburst decay) in the *XMM-Newton* and *NuSTAR* observations have different frequencies compared to the ones reported earlier (50 and 220 mHz). We also noticed that the PSDs of the observations during 2015 outburst have a different overall shape when compared to the PSDs during the 2016 Type-I outburst (*this work*) and the previously reported PSDs during two different Type-II outbursts from *Ginga* (Takeshima et al. 1994) and *RXTE* (Qu et al. 2005; Caballero-García, M. D. et al. 2016). This variable nature of the PSD directly indicates that the factors contributing towards aperiodic variability in the source vary over time.

The 2015 *XMM-Newton* and *NuSTAR* observations show a QPO at 40 mHz (Figs A5 and A6) while the 2016 *NuSTAR* observations show twin QPOs at 2.5 mHz and 18 mHz (Fig. A7). Twin QPOs have been reported in V 0332+53 (Qu et al. 2005) and in GX 304–1 (Devasia et al. 2011). However, the twin QPOs in V 0332+53 reported before have centroid frequencies of 50 and 220 mHz, where 220 mHz is the spin period of the NS. Qu et al. (2005) proposed that inhomogeneous accretion flow at the polar caps results in coupling between the spin-variability and noise-variability in the PDS, which could lead to the appearance of QPO at NS spin frequency. In GX 304 − 1, the second QPO was a harmonic of the first, which is not the case here.

Spectra from all the observations could be modelled with a soft-blackbody component and a power-law-based comptonization component (Table 4). The 2015 observations were performed when the source was ≥5 time brighter than during the 2016 observations. The higher QPO frequency during a high X-ray flux state favours the inner accretion disc origin of QPO, which might move closer to the neutron star, resulting in an enhanced Keplerian orbital frequency. Following the relations $r \propto \dot{M}^{-2/7}$ and Keplerian relation of $\nu \propto r^{-3/2}$, we get $\nu \propto \dot{M}^{3/7}$. Under this argument, an increase in QPO frequency to a factor of $\sim 2$ (from 18 to 40 mHz) requires $\dot{M}$ ($L_X$) to scale up to a factor of $\sim 5$, which is close to the measured X-ray flux from the spectral analysis. However, a similar argument for an increase in QPO frequency from 2.5 to 40 mHz would require a factor of $\geq 600$ increase in $\dot{M}$. Thus, the 40 mHz QPO observed

during the 2015 outburst and 18 mHz QPO observed during the 2016 outburst are likely of similar origin, while the 2.5 mHz QPO is likely of a different origin. The *Q*-factor of 18 mHz QPO present at low flux is also about a factor of $\gtrsim 2$ higher that of the 40 mHz QPO present at a high flux (Table 7). A similar increment in the *Q*-factor with decreasing flux has also been observed for the 220 mHz QPO by Qu et al. (2005).

A careful consideration of the estimate of Alfven radius from Lamb, Pethick & Pines (1989) in Section 4.5, however, shows that the 40 mHz QPO could be explained with BFM, and a shift in QPO frequency to 18 mHz is unlikely to be due to change in luminosity. Moreover, this interpretation of the 18 and 40 mHz having a common origin contrasts with the observation of Qu et al. (2005), where it was shown that the QPO centroid frequency does not evolve with source flux.

## 4.4 Association of QPO with the soft excess

XRPs sufficiently away from the galactic plane are known to exhibit soft excess in their energy spectrum and is usually associated with the X-ray emission from the NS reprocessed by the inner accretion disc (Paul et al. 2002, Hickox, Narayan & Kallman 2004). It is usually modelled with a low temperature ($kT \sim$ 100–200 eV) blackbody component. The idea that both soft excess and QPOs in XRPs are considered to originate from the inner accretion disc motivated us to look for patterns in the QPO strength in the soft-excess energy band. *XMM-Newton*/PN is the most suitable detector for such a study, as it has low energy coverage till 0.5 keV to detect the soft excess and a relatively good effective area for high significance detection of QPO. However, sources that exhibit both QPO in the light curve and soft excess in the spectrum were needed to perform such a study.

Out of the five sources in which we detected *XMM-Newton* observations, only 4U 1626–67 satisfies this criterion. Despite soft-excess being also detected in V 0332+53 and Cen X−3, the blackbody dominant spectral band is outside the sensitive instrument energy band to perform QPO rms estimation. We modelled the soft excess in 4U 1626–67 with a blackbody component of $kT_{BB} \sim$0.3 keV. The black body contribution is expected to peak around 0.8 keV ($\sim$2.8 $kT_{BB}$). Incidentally, QPO also shows high rms values of about 20 per cent in the 0.5–3 keV spectral band in 4U 1626–67 (Fig. 1). An alternate interpretation is that the QPO rms is consistently high in the 0.5–10 keV with an abrupt drop in 3–5.7 keV, which seems unlikely when looking at it together with QPO rms from other wavelengths (See Section 3.1) and the *RXTE*/PCA observation (Fig. A2).

However, apart from the soft excess, 1–3 keV also contains the Ne emission complex (See Fig. 2), the origin of which is believed to be the O/Ne rich accretion disc of 4U 1626–67 (Schulz et al. 2001). To check if the QPO rms show any anomaly in the energy range corresponding to the Neon emission complex, we calculated the QPO rms in 0.5–0.9, 0.9–1.1, and 1.1–3 keV energy bands, and there seems to be no significant rise in the QPO rms peculiar to the Neon spectral range in the two *XMM-Newton* observations (Fig. 7). The QPO rms as a function of energy from combined multiple *NICER* observations also show that the QPO rms is maximum in 1.3–1.9 keV, i.e, neither at the soft-excess energy band nor at the Neon line energy band (Fig. 2). Therefore, we found no evidence to associate the origins of soft-excess and QPO.

## 4.5 Applicability of KFM and BFM

The KFM treats QPO as the NS emission modulated by the inhomogeneous matter orbiting at Keplerian orbit in the inner accretion
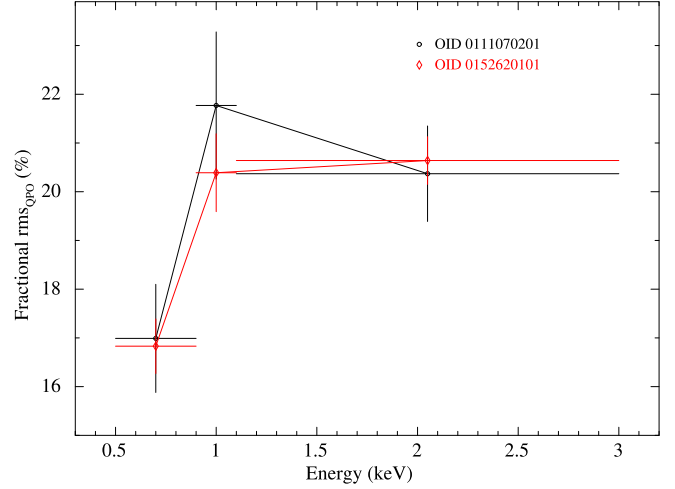


**Figure 7.** QPO rms in three different energy ranges of two *XMM-Newton* observations of 4U 1626 − 67. The QPO rms shows a rise throughout the 0.9–3.0 keV band in both observations.

disc. KFM imposes the condition $\nu_{NS} < \nu_{QPO}$, and based on this the applicability of KFM is invalid on four of the five QPOs we detected (See Table 8). It could be applicable in XTE J1858+034, which gives the inner accretion disc orbital frequency as 196 mHz. But considering that soft X-rays are vulnerable to absorption from cold matter compared to hard X-rays, the QPO rms is expected to peak at lower energies, i.e. exhibiting anticorrelation with energy. However, a strong positive correlation is exhibited by XTE J1858 + 034 between QPO rms and photon energy in both the *NuSTAR* (this work) and *RXTE*/PCA (Mukherjee et al. 2006), with the QPO rms reaching about 10 per cent in 15–25 keV in the *NuSTAR* observation.

KFM is therefore not apt to explain the QPOs we observed. From the observed QPO frequency and the pulsar spin frequency, we estimated the orbital frequency of the inner accretion disc in each case (Table 8). Both KFM and BFM also predict the QPO centroid frequency to vary with the X-ray luminosity, which is not generally observed in XRPs (Finger 1998; Raichur & Paul 2008). Exceptions are A 0535 + 262 (Finger et al. 1996; Finger 1998; Ma et al. 2022) and XTE J1858 + 034 (Mukherjee et al. 2006), where, a positive correlation of the QPO frequency with X-ray flux was observed. We found such a variation in V 0332+53, where the QPO centroid frequency is almost doubled when the X-ray flux increased $\sim$5 times (See the discussion in Section 4.3).

The inner accretion disc is expected to terminate at the Alfven radius ($r_M$), and $r_M$ (Lamb et al. 1989; Becker et al. 2012) is given by

$$r_M = 2.73 \times 10^7 \text{cm} \left(\frac{\Lambda}{0.1}\right) \left(\frac{M_\star}{1.4M_\odot}\right)^{1/7} \left(\frac{R_\star}{10 \text{ km}}\right)^{10/7}$$
$$\times \left(\frac{B_\star}{10^{12} \text{ G}}\right)^{4/7} \left(\frac{L_x}{10^{37}\text{ergs s}^{-1}}\right)^{-2/7} \quad (1)$$

$\Lambda$ is a constant, and $\Lambda = 1$ for spherical accretion, and $\Lambda \approx 0.22\alpha^{18/69}$ for disc accretion, where $\alpha$ is the alpha-disc parameter. $\Lambda = 0.1$ is a fair approximation for typical values of $\alpha$ between 0.01–0.1 (Becker et al. 2012). $M_\star$ is the mass of the NS, $R_\star$ is the radius of NS, $B_\star$ is the magnetic field at the surface of the NS, and $L_x$ is the X-ray luminosity of the source. We checked the difference in $r_M$ predicted by equation (1) from the inner accretion radius ($r_{BFM}$)

**Table 8.** Characteristics of the observed QPOs and applicability of Keplerian and BFMs.

| Source | Type | $\nu_{QPO}$ in mHz | E-relation | $\nu_{orb}$ (inner acc. disc) in mHz | | Unabsorbed Flux$_{2-20keV}$ in $10^{-10}$ ergs s$^{-1}$ cm$^{-2}$ | inner acc. disc radius in km | | | References[⊤] |
|---|---|---|---|---|---|---|---|---|---|---|
| | | | | KFM[†] | BFM[§] | | $r_{KFM}$ | $r_{BFM}$ | $r_M$ | |
| 4U 1626–67 | Persistent | 48 | + ve | N.A | 178 | 2.8 | – | 5305 | 1055 | Staubert et al. (2019) |
| IGR J19294 + 1816 | Transient | 30 | + ve | N.A | 113 | 4.0 | – | 7182 | 6616 | Staubert et al. (2019) |
| V 0332+53 | Transient | 2.5 | nil | N.A | 230 | 6.1–7.5 | – | 4478 | 5386–5713 | Staubert et al. (2019) |
| | | 18 | nil | N.A | 245 | 6.1–7.5 | – | 4287 | 5386–5713 | Staubert et al. (2019) |
| | | 40 | nil | N.A | 267 | 29.1–124.8 | – | 4049 | 2411-3656 | Staubert et al. (2019) |
| Cen X–3 | Persistent | 30 | + ve | N.A | 238 | 67.1 | – | 4371 | 2775 | Staubert et al. (2019) |
| XTE J1858 + 034 | Transient | 185 | + ve | 185 | 190 | 10.4 | 5170 | 5088 | 5363 | Malacaria et al. (2021) |

[†] $\nu_{orb} = \nu_{QPO}$. KFM is not applicable if $\nu_{QPO} < \nu_{NS}$ (denoted by N.A).
[§] $\nu_{orb} = \nu_{QPO} + \nu_{NS}$.
[⊤] References for distance to the source and magnetic field strength.

predicted by BFM, given by

$$r_{BFM} = \left( \frac{GM_{NS}}{4\pi^2(\nu_{QPO} + \nu_{NS})^2} \right)^{1/3} \qquad (2)$$

The results are summarized in Table 8. The BFM predicted inner accretion radius and the Alfven radius are within a factor of 1.1 in IGR J19294+1816, XTE J1858+034, and the 40 mHz QPO in V 0332+53. However, they are off by a factor of 1.5 or less in the 2.5 mHz and 18 mHz QPOs in V 0332+53, and by a factor of 1.5 or more in 4U 1626–67 and Cen X–3. BFM could therefore explain the QPOs only in IGR J19294+1816, V 0332+53 (40 mHz), and XTE J1858 + 034. The estimate of Alfven radius from equation (1) is also, however, bound to have uncertainties from various variables.

Beyond KFM and BFM, we also acknowledge the existence of other QPO models, for instance, the magnetically driven disc precession model (Shirakawa & Lai 2002). However, this model does not predict the energy dependence of QPO rms.

### 4.6 QPOs in other accretion-powered X-ray sources

Besides XRPs, black hole binaries (BHBs) and low magnetic field ($10^8$–$10^9$ G) neutron stars in low-mass X-ray binaries (NSBs) are two other classes of accretion-powered X-ray binaries containing primary compact stellar objects with a mass of the order of $M_\odot$, that exhibits QPOs which has been well studied. The QPOs exhibited by BHBs are broadly classified into two types based on their centroid frequency, namely the low-frequency QPOs (LFQPOs; $0.1 - 30$ Hz) and the high-frequency QPOs (HFQPOs; $>30$ Hz). HFQPOs in BHBs like the QPOs exhibited by XRP are also a transient phenomena (Belloni, Sanna & Méndez 2012). NSBs exhibit QPOs at kHz frequencies, known as kHz QPOs (they sometimes appear in pairs, and are then known as twin kHz QPOs). Due to the centroid frequency being close to the Keplerian frequency of their inner accretion discs, the kHz QPOs in NSBs and HFQPOs in BHBs are generally associated with the accretion disc (Remillard & McClintock 2006). Moreover, BHBs and NSBs usually exhibit different spectral states like high-soft state (high luminosity and soft spectrum), low-hard state and intermediate state. The kHz QPOs in NSBs and HFQPOs in BHBs are usually observed during the soft states (Motta et al. 2017), which are generally associated with the accretion disc. Considering their connection with the accretion disc, the mHz QPOs in XRPs, kHz QPOs in NSBs and HFQPOs in BHBs could be discussed in the same context.

The twin kHz QPOs in NSBs are usually explained by two models; the sonic point BFM (Miller, Lamb & Psaltis 1998) and the relativistic precession model (Stella & Vietri 1998). The relativistic precession model interprets the HF kHz QPO from the inner accretion disc and LF kHz QPO as relativistic precession modes at that orbit. The sonic point BFM interprets the high-frequency kHz QPO to be related to the clumps in the innermost accretion disc and the LF kHz QPO as the beat frequency between neutron star spin and the HF kHz QPO. The sonic point model is a combination of the KFM and BFM employed in XRPs. If the sonic point model is employed to explain the twin QPOs (2 and 18 mHz) observed in two *NuSTAR* observations of V 0332+53, the model predicts a spin frequency of NS around 20 mHz, while the true value stands at 220 mHz.

In general, QPOs in XRPs (*this work*), HFQPOs (Morgan, Remillard & Greiner 1997, van der Klis 2000) and kHz QPOs (Berger et al. 1996, Strohmayer et al. 1996, Zhang et al. 1996, Wijnands et al. 1997) exhibit a positive correlation of QPO rms with photon energy. A key aspect that sets the QPOs in XRPs apart is their QPO

rms that regularly goes over 10 per cent up to 30 per cent (this work) when compared to < 20 per cent in kHz QPOs (Zhang et al. 1996, Wijnands et al. 1997) and even lower values for the rarely detected transient HFQPOs (Belloni et al. 2012).

## 5 CONCLUSIONS

We analysed 99 *XMM-Newton* and *NuSTAR* observations of 29 accreting XRPs and searched for the presence of mHz QPOs in them. We detected QPOs in six *XMM-Newton* observations and three *NuSTAR* observations and estimated the variation of QPO properties with photon energy. The Magnetospheric beat frequency model (BFM) is favourable over the KFM in IGR J19294+1816, V 0332+53 (40 mHz) and XTE J1858 + 034. Twin QPOs were detected in the *NuSTAR* observation of V 0332+53.

## ACKNOWLEDGEMENTS

## DATA AVAILABILITY

All the data underlying this research work is publicly available in NASA's HEASARC Data archive.

## REFERENCES

Aftab N., Paul B., Kretschmar P., 2019, ApJS, 243, 29
Alpar M. A., Shaham J., 1985, Nature, 316, 239
Arnaud K. A., 1996 Astronomical Data Analysis Software and Systems V, 101, 17, Astronomical Society of the Pacific Conference Series, https://ui.adsabs.harvard.edu/abs/1996ASPC..101...17A/abstract
Becker P. et al., 2012, A&A, 544, A123
Belloni T. M., Sanna A., Méndez M., 2012, MNRAS, 426, 1701
Belloni T., Hasinger G., 1990, A&A, 230, 103
Berger M. et al., 1996, ApJ, 469, L13
Beri A., Jain C., Paul B., Raichur H., 2014, MNRAS, 439, 1940
Beri A., Paul B., Dewangan G. C., 2018, MNRAS, 475, 999
Caballero-García, M. D. et al., 2016, A&A, 589, A9
Camero-Arranz A., Pottschmidt K., Finger M., Ikhsanov N., Wilson-Hodge C., Marcu D., 2012, A&A, 546, A40
Chakrabarty D., 1998, ApJ, 492, 342
Chakrabarty D., Homer L., Charles P. A., O'Donoghue D., 2001, ApJ, 562, 985
Coburn W., Heindl W. A., Rothschild R. E., Gruber D. E., Kreykenbohm I., Wilms J., Kretschmar P., Staubert R., 2002, ApJ, 580, 394
Devasia J., James M., Paul B., Indulekha K., 2011, MNRAS, 417, 348
Domcek V. et al., 2019, Astron. Telegram, 13215, 1
Doroshenko V., Tsygankov S. S., Mushtukov A. A., Lutovinov A. A., Santangelo A., Suleimanov V. F., Poutanen J., 2017, MNRAS, 466, 2143
Elshamouty K. G., Heinke C. O., Chouinard R., 2016, MNRAS, 463, 78

Finger M. H., 1998, Adv. Space Res., 22, 1007
Finger M., Wilson R., Harmon B., 1996, ApJ, 459, 288
Gendreau K. C. et al., 2016, in conference proceeding Space Telescopes and Instrumentation 2016: Ultraviolet to Gamma Ray SPIE, 9905P. 420
Harrison F. A. et al., 2013, ApJ, 770, 103
Hickox R. C., Narayan R., Kallman T. R., 2004, ApJ, 614, 881
Jahoda K., Markwardt C. B., Radeva Y., Rots A. H., Stark M. J., Swank J. H., Strohmayer T. E., Zhang W., 2006, ApJS, 163, 401
Jain C., Paul B., Dutta A., 2010, MNRAS, 403, 920
James M., Paul B., Devasia J., Indulekha K., 2010, MNRAS, 407, 285
Kaastra J., Bleeker J., 2016, A&A, 587, A151
Kaur R., Paul B., Kumar B., Sagar R., 2008, ApJ, 676, 1184
Klis M. V. D., 1997, in, Astronomical Time Series. Springer, Dordrechtp.121
Kommers J. M., Chakrabarty D., Lewin W. H., 1998, ApJ, 497, L33
Lamb F., Pethick C., Pines D., 1973, ApJ , 184 , 271, https://ui.adsabs.harvard.edu/abs/1973ApJ...184..271L/abstract
Liu Q. et al., 2022, MNRAS, 516, 5579
Ma R. et al., 2022, MNRAS, 517, 1988
Malacaria C. et al., 2021, ApJ, 909, 153
Malacaria C. et al., 2024, A&A, 681, A25
Mandal M., Pal S., 2021, preprint (arXiv:2101.09250)
Miller M. C., Lamb F. K., Psaltis D., 1998, ApJ, 508, 791
Morgan E. H., Remillard R. A., Greiner J., 1997, ApJ, 482, 993
Motta S. E., Rouco Escorial A., Kuulkers E., Muñoz-Darias T., Sanna A., 2017, MNRAS, 468, 2311
Mowlavi N. et al., 2006, A&A, 451, 187
Mukherjee U., Bapna S., Raichur H., Paul B., Jaaffrey S., 2006, JA&A, 27, 25
Naik S., Paul B., 2012, Bull. Astr. Soc. India, 40, 503
Nespoli E., Reig P., 2011, A&A, 526, A7
Paul B., Nagase F., Endo T., Dotani T., Yokogawa J., Nishiuchi M., 2002, ApJ, 579, 411
Paul B., Rao A. R., 1998, A&A, 337, 815
Petterson J. A., 1978, ApJ, 224, 625
Qu J. L., Zhang S., Song L. M., Falanga M., 2005, ApJL, 629, L33
Raichur H., Paul B., 2008, ApJ, 685, 1109
Raman G., Paul B., Bhattacharya D., 2021, MNRAS, 508, 5578
Reig P., Negueruela I., Papamastorakis G., Manousakis A., Kougentakis T., 2005, A&A, 440, 637
Reig P., Nespoli E., 2013, A&A, 551, A1
Remillard R. A., McClintock J. E., 2006, ARA&A, 44, 49
Rodes-Roca J. J., Bernabeu G., Magazzù A., Torrejón J. M., Solano E., 2018, MNRAS, 476, 2110
Rodriguez J., Tomsick J. A., Bodaghee A., Zurita Heras J. A., Chaty S., Paizis A., Corbel S., 2009, A&A, 508, 889
Sanjurjo-Ferrín G., Torrejón J. M., Postnov K., Oskinova L., Rodes-Roca J. J., Bernabeu G., 2021, MNRAS, 501, 5892
Schulz N. S., Chakrabarty D., Marshall H. L., Canizares C. R., Lee J. C., Houck J., 2001, ApJ, 563, 941
Sharma R., Jain C., Paul B., 2023b, MNRAS, 526, L35
Sharma R., Jain C., Rikame K., Paul B., 2023a, MNRAS, 519, 1764
Shinoda K., Kii T., Mitsuda K., Nagase F., Tanaka Y., Makishima K., Shibazaki N., 1990, PASJ, 42, L27
Shirakawa A., Lai D., 2002, ApJ, 565, 1134
Staubert R. et al., 2019, A&A, 622, A61
Stella L., Vietri M., 1998, ApJ, 492, L59
Stella L., White N. E., Davelaar J., Parmar A. N., Blissett R. J., van der Klis M., 1985, ApJ, 288, L45
Strohmayer T. E., Zhang W., Swank J. H., Smale A., Titarchuk L., Day C., Lee U., 1996, ApJ, 469, L9
Strüder L. et al., 2001, A&A, 365, L18
Suchy S. et al., 2008, ApJ, 675, 1487
Takeshima T., Corbet R. H. D., Marshall F. E., Swank J., Chakrabarty D., 1998, IAU Circ., 6826, 1
Takeshima T., Dotani T., Mitsuda K., Nagase F., 1994, ApJ, 436, 871
Tamba T., Odaka H., Tanimoto A., Suzuki H., Takashima S., Bamba A., 2023, ApJ, 944, 9
Tsygankov S. S. et al., 2021, ApJ, 909, 154

Tsygankov S. S., Doroshenko V., Mushtukov A. A., Lutovinov A. A., Poutanen J., 2019a, A&A, 621, A134

Tsygankov S. S., Doroshenko V., Mushtukov A. A., Lutovinov A. A., Poutanen J., 2019b, A&A, 621, A134

Tsygankov S. S., Wijnands R., Lutovinov A. A., Degenaar N., Poutanen J., 2017, MNRAS, 470, 126

van der Klis M., 1989, eds.Ögelman H., van den Heuvel E. P. J., in Timing Neutron Stars, NATO Advanced Study Institute (ASI) Series C, Dordrecht, 262,27

van der Klis M., 2000, ARA&A, 38, 717

Vybornov V., Doroshenko V., Staubert R., Santangelo A., 2018, A&A, 610, A88

Wijnands R. et al., 1997, ApJ, 490, L157

Zhang W., Lapidus I., White N. E., Titarchuk L., 1996, ApJ, 469, L17

## APPENDIX A: QPO FITS
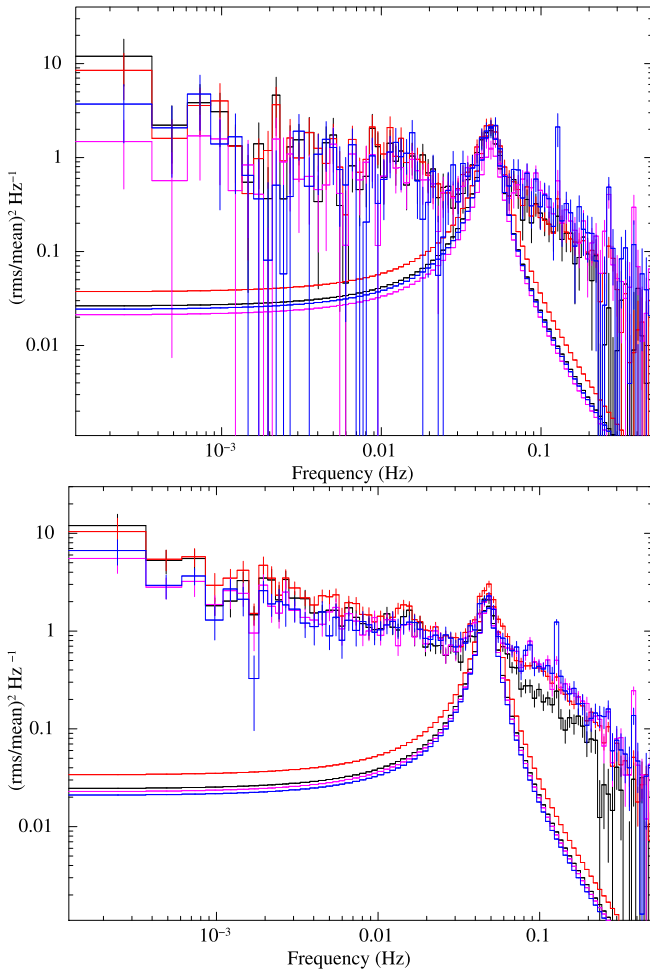
**Figure A1.** The *XMM-Newton*/PN PSD of 4U 1626–67 in different energy bands (0.5–1 keV in black, 1–3 keV in red, 3–5.7 keV in magenta, and 5.7−10.0 keV in blue) of OID 0152620101 (Top) and OID 111070201 (Bottom). QPO at 40 mHz is fitted with Lorentzian profile.
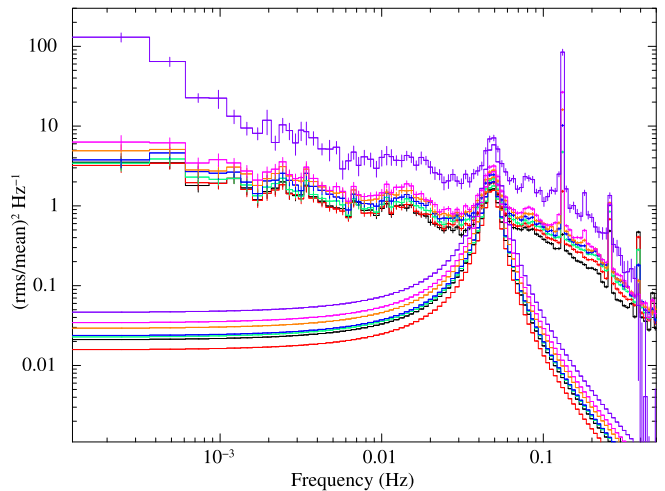


**Figure A2.** The *RXTE*/PCA PSD of 4U 1626–67 in different energy bands (2.02−6.70 keV in black, 6.7−8.5 keV in red, 8.5−11.1 keV in green, 11.1−13.0 keV in blue, 13.0−15.4 keV in orange, 15.4−20.2 keV in magenta and 20.2−60.0 keV in purple). The QPO at 48 mHz is fitted with a `Lorentzian` profile.
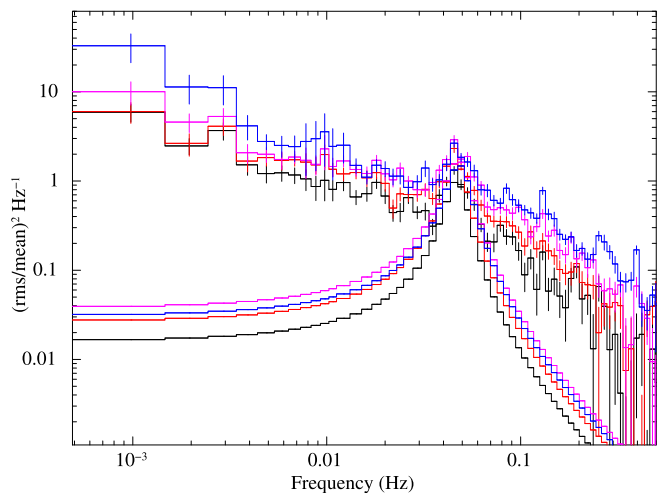


**Figure A3.** The *NICER* PSD of 4U 1626–67 in different energy bands (0.5−0.9 keV in black, 0.9−1.3 keV in red, 1.3−1.9 keV in magenta, 1.9−3.5 keV in blue). The QPO at 48 mHz is fitted with a `Lorentzian` profile.
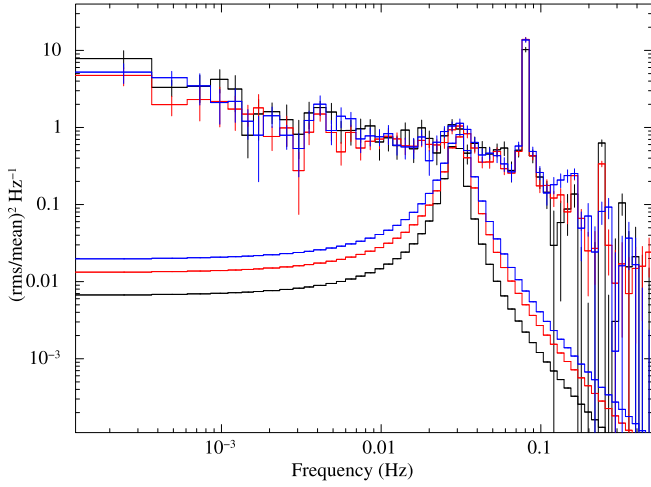
**Figure A4.** The *XMM-Newton*/PN PSD of IGR J19296 + 1816 in different energy bands (0.5–3 keV in black, 3–5.7 keV in red, and 5.7–10 keV in blue). The QPO at 30 mHz is fitted with a `Lorentzian` profile.
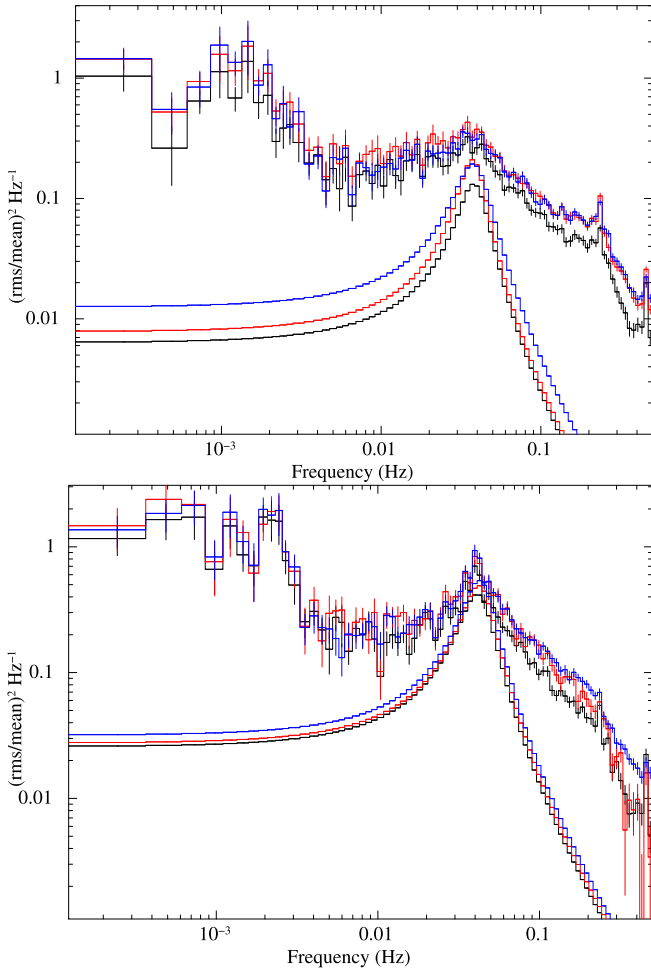
**Figure A5.** The *XMM-Newton*/PN PSD of V 0332+53 in different energy bands (0.5–3 keV in black, 3–5.7 keV in red, and 5.7–10 keV in blue) of OID 0763470301 (Top) and OID 0763470401 (Bottom). QPO at 40 mHz is fitted with a `Lorentzian` profile.
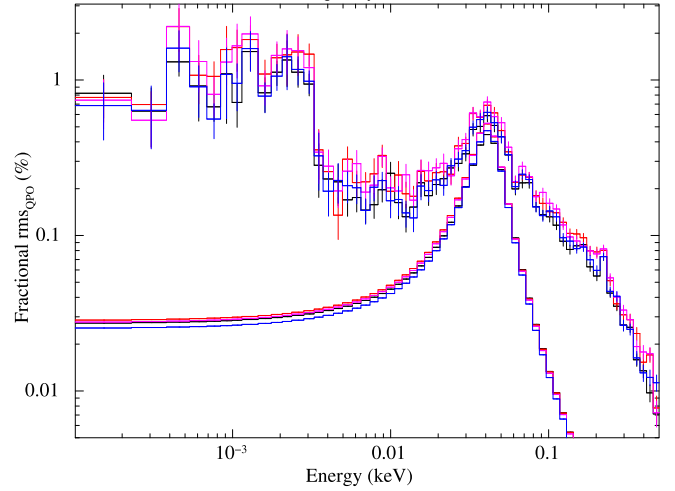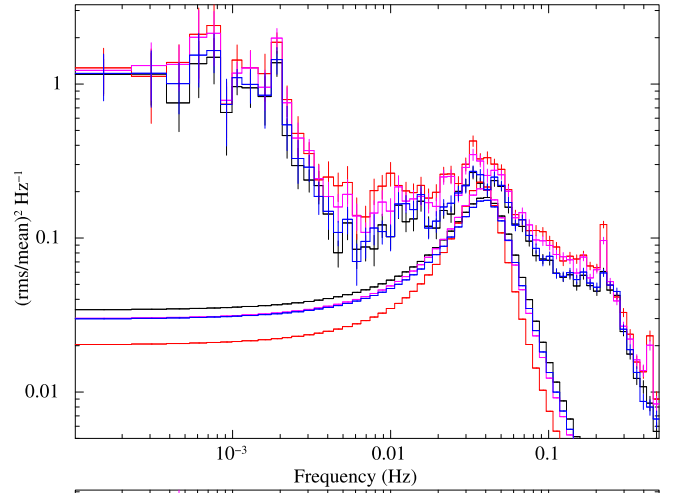
**Figure A6.** The *NuSTAR* PSD of V 0332+53 in different energy bands (3–6 keV in black, 6–8.5 keV in red, 8.5–11.5 keV in magenta, and 11.5–60 keV in blue) of OID 80102002004 (Top) and OID 80102002006 (Bottom). QPO at 40 mHz is fitted with a `Lorentzian` profile.
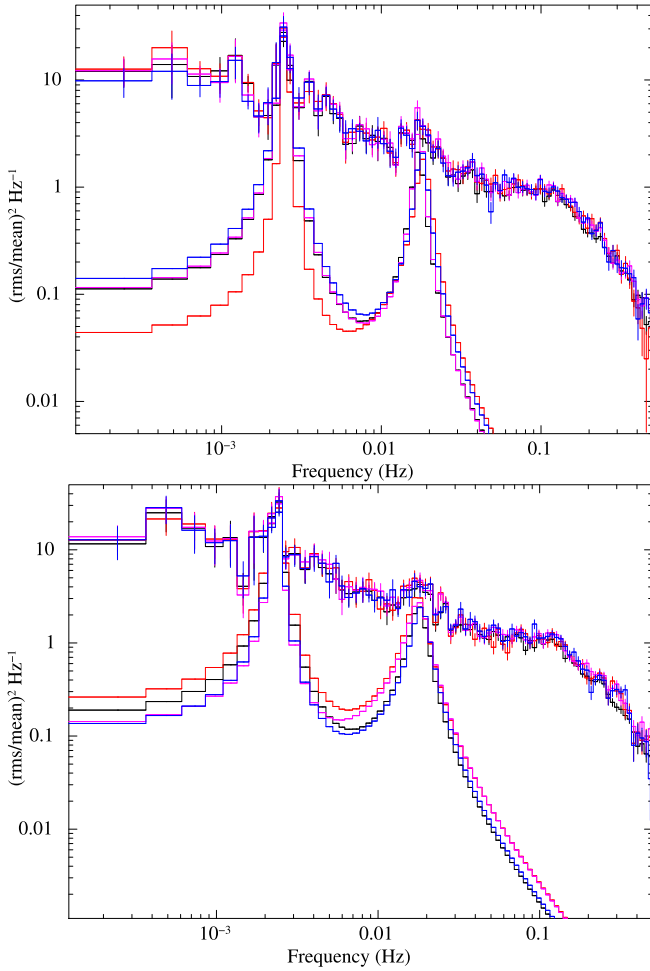
**Figure A7.** The *NuSTAR* PSD of V 0332+53 in different energy bands (3–8 keV in black, 8–10 keV in red, 10–15 keV in magenta, and 15–25 keV in blue). Twin QPOs at 2.5 mHz and 18 mHz were fitted with two `Lorentzian` profiles.



**Figure A8.** The *XMM-Newton*/PN PSD of Cen X–3 in three different energy bands (0.5–3 keV in black, 3–5.7 keV in red, and 5.7–10 keV in blue). QPO at 30 mHz is fitted with `Lorentzian` profile.



**Figure A9.** The *NuSTAR* PSD of XTE J1858 + 034 in four different energy bands (3–8 keV in black, 8–10 keV in red, 10–15 keV in magenta, and 15–25 keV in blue). QPO at ∼185 mHz was fitted with a `Lorentzian` profile.

## APPENDIX B: OBSERVATIONS
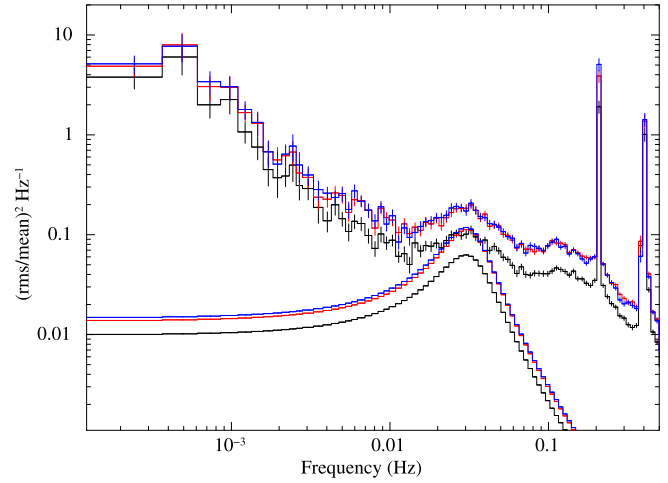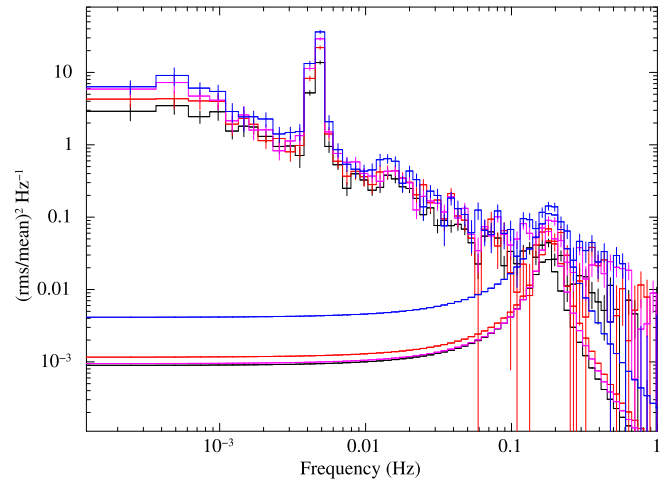
**Table B1.** Observations log.

| Sl no. | Source | Observatory/Instrument | Obs. ID | Observation mode | Observation duration (ks) |
|---|---|---|---|---|---|
| 1 | 1A 0535 + 262 | *XMM-Newton*/PN | 0674180101 | PrimeFullWindow | 58 |
| 2 | | *NuSTAR*/FPMA,B | 80001016002 | - | 43 |
| 3 | | *NuSTAR*/FPMA,B | 80001016004 | - | 56 |
| 4 | | *NuSTAR*/FPMA,B | 90401370001 | - | 118 |
| 5 | 2S 1553–542 | *NuSTAR*/FPMA,B | 90101002002 | - | 50 |
| 6 | 4U 0115 + 63 | *NuSTAR*/FPMA,B | 90102016002 | - | 38 |
| 7 | | *NuSTAR*/FPMA,B | 90102016004 | - | 41 |
| 8 | 4U 1538–522 | *XMM-Newton*/PN | 0152780201 | PrimeFullWindow | 79 |
| 9 | | *NuSTAR*/FPMA,B | 30201028002 | - | 85 |
| 10 | 4U 1626–67 | *XMM-Newton*/PN | 0111070201 | PrimeSmallWindow | 16 |
| 11 | | *XMM-Newton*/PN | 0152620101 | PrimeSmallWindow | 84 |
| 12 | | *XMM-Newton*/PN | 0764860101 | FastTiming | 54 |
| 13 | | *NuSTAR*/FPMA,B | 30101029002 | - | 114 |
| 14 | | *RXTE*/PCA | P10101 | Good Xenon | 395 |
| 15 | 4U 1700–37 | *XMM-Newton*/PN | 0600950101 | PrimeFullWindow | 50 |
| 16 | | *NuSTAR*/FPMA,B | 30101027002 | - | 74 |
| 17 | 4U 1901 + 03 | *NuSTAR*/FPMA,B | 90501305001 | - | 44 |
| 18 | | *NuSTAR*/FPMA,B | 90501324002 | - | 102 |
| 19 | | *NuSTAR*/FPMA,B | 90502307002 | - | 38 |
| 20 | | *NuSTAR*/FPMA,B | 90502307004 | - | 55 |
| 21 | 4U 1907 + 09 | *XMM-Newton*/PN | 0555410101 | FastTiming | 21 |
| 22 | | *NuSTAR*/FPMA,B | 30401018002 | - | 154 |
| 23 | 4U 2206 + 54 | *XMM-Newton*/PN | 0650640101 | PrimeLargeWindow | 75 |
| 24 | | *NuSTAR*/FPMA,B | 30201015002 | - | 108 |
| 25 | Cen X–3 | *XMM-Newton*/PN | 0111010101 | PrimeSmallWindow | 67 |
| 26 | | *XMM-Newton*/PN | 0400550201 | FastTiming | 80 |
| 27 | | *NuSTAR*/FPMA,B | 30101055002 | - | 39 |
| 28 | Cep X–4 | *NuSTAR*/FPMA,B | 80002016002 | - | 79 |
| 29 | | *NuSTAR*/FPMA,B | 80002016004 | - | 76 |
| 30 | EXO 2030 + 375 | *XMM-Newton*/PN | 0745240201 | FastTiming | 31 |
| 31 | | *NuSTAR*/FPMA,B | 90201029002 | - | 117 |
| 32 | | *NuSTAR*/FPMA,B | 90701336002 | - | 50 |
| 33 | GRO J1008–57 | *NuSTAR*/FPMA,B | 80001001002 | - | 32 |
| 34 | GRO J1744–28 | *XMM-Newton*/PN | 0506291201 | FastTiming | 38 |
| 35 | | *XMM-Newton*/PN | 0729560401 | FastTiming | 82 |
| 36 | | *NuSTAR*/FPMA,B | 80002017002 | - | 67 |
| 37 | | *NuSTAR*/FPMA,B | 80202027002 | - | 56 |
| 38 | GX 301–2 | *XMM-Newton*/PN | 0555200301 | FastTiming | 59 |
| 39 | | *XMM-Newton*/PN | 0555200401 | FastTiming | 47 |
| 40 | | *NuSTAR*/FPMA,B | 30001041002 | - | 51 |
| 41 | | *NuSTAR*/FPMA,B | 30101042002 | - | 53 |
| 42 | GX 304–1 | *NuSTAR*/FPMA,B | 90401326002 | - | 108 |
| 43 | IGR J16393-4643 | *XMM-Newton*/PN | 0206380201 | PrimeLargeWindow | 9 |
| 44 | | *XMM-Newton*/PN | 0604520201 | PrimeSmallWindow | 19 |
| 45 | | *NuSTAR*/FPMA,B | 30001008002 | - | 96 |
| 46 | IGR J17329–2731 | *XMM-Newton*/PN | 0795711701 | FastTiming | 37 |
| 47 | | *NuSTAR*/FPMA,B | 90301012002 | - | 38 |
| 48 | IGR J17544–2619 | *XMM-Newton*/PN | 0679810401 | PrimeSmallWindow | 15 |
| 49 | | *XMM-Newton*/PN | 0679810501 | PrimeSmallWindow | 15 |
| 50 | | *XMM-Newton*/PN | 0744600101 | PrimeFullWindow | 135 |
| 51 | | *NuSTAR*/FPMA,B | 30002003003 | - | 50 |
| 52 | IGR J18027–2016 | *XMM-Newton*/PN | 0206380601 | PrimeLargeWindow | 10 |
| 53 | | *XMM-Newton*/PN | 0745060401 | PrimeFullWindow | 43 |
| 54 | | *XMM-Newton*/PN | 0745060501 | PrimeFullWindow | 16 |
| 55 | | *XMM-Newton*/PN | 0745060601 | PrimeFullWindow | 17 |
| 56 | | *XMM-Newton*/PN | 0745060701 | PrimeFullWindow | 14 |
| 57 | | *XMM-Newton*/PN | 0745060801 | PrimeFullWindow | 17 |
| 58 | | *NuSTAR*/FPMA,B | 30101049002 | - | 85 |
| 59 | IGR J19294 + 1816 | *XMM-Newton*/PN | 0841190101 | PrimeFullWindow | 67 |
| 60 | | *NuSTAR*/FPMA,B | 90401306002 | - | 79 |
| 61 | | *NuSTAR*/FPMA,B | 90401306004 | - | 79 |
| 62 | KS1947 + 300 | *XMM-Newton*/PN | 0727961201 | FastTiming | 12 |
| 63 | | *NuSTAR*/FPMA,B | 80002015002 | - | 38 |
| 64 | | *NuSTAR*/FPMA,B | 80002015004 | - | 42 |
| 65 | | *NuSTAR*/FPMA,B | 80002015006 | - | 56 |
| 66 | RX J0520.5–6932 | *XMM-Newton*/PN | 0701990101 | PrimeFullWindow | 20 |

**Table B1** *– continued*

| Sl no. | Source | Observatory/Instrument | Obs. ID | Observation mode | Observation duration (ks) |
|---|---|---|---|---|---|
| 67 | | *XMM-Newton*/PN | 0729560201 | FastTiming | 2 |
| 68 | | *XMM-Newton*/PN | 0729560301 | FastTiming | 10 |
| 69 | | *NuSTAR*/FPMA,B | 80001002002 | - | 54 |
| 70 | | *NuSTAR*/FPMA,B | 80001002004 | - | 66 |
| 71 | SMC X–1 | *XMM-Newton*/PN | 0784570201 | FastTiming | 19 |
| 72 | | *XMM-Newton*/PN | 0784570301 | FastTiming | 19 |
| 73 | | *XMM-Newton*/PN | 0784570401 | FastTiming | 21 |
| 74 | | *XMM-Newton*/PN | 0784570501 | FastTiming | 19 |
| 75 | | *XMM-Newton*/PN | 0893400101 | PrimeSmallWindow | 21 |
| 76 | | *XMM-Newton*/PN | 0893400301 | PrimeSmallWindow | 22 |
| 77 | | *NuSTAR*/FPMA,B | 30202004002 | - | 42 |
| 78 | | *NuSTAR*/FPMA,B | 30202004004 | - | 42 |
| 79 | | *NuSTAR*/FPMA,B | 30202004006 | - | 38 |
| 80 | | *NuSTAR*/FPMA,B | 30202004008 | - | 43 |
| 81 | SMC X–2 | *XMM-Newton*/PN | 0770580701 | FastTiming | 8 |
| 82 | | *NuSTAR*/FPMA,B | 90101017002 | - | 48 |
| 83 | | *NuSTAR*/FPMA,B | 90102014002 | - | 48 |
| 84 | | *NuSTAR*/FPMA,B | 90102014004 | - | 50 |
| 85 | | *XMM-Newton*/PN | 0770580901 | PrimeSmallWindow | 31 |
| 86 | V 0332+53 | *XMM-Newton*/PN | 0506190101 | PrimeFullWindow | 36 |
| 87 | | *XMM-Newton*/PN | 0763470301 | FastTiming | 32 |
| 88 | | *XMM-Newton*/PN | 0763470401 | FastTiming | 31 |
| 89 | | *NuSTAR*/FPMA,B | 80102002004 | – | 41 |
| 90 | | *NuSTAR*/FPMA,B | 80102002006 | – | 38 |
| 91 | | *NuSTAR*/FPMA,B | 80102002008 | – | 38 |
| 92 | | *NuSTAR*/FPMA,B | 80102002010 | - | 44 |
| 93 | | *NuSTAR*/FPMA,B | 90202031002 | - | 44 |
| 94 | | *NuSTAR*/FPMA,B | 90202031004 | - | 44 |
| 95 | X Persei | *XMM-Newton*/PN | 0151380101 | PrimeFullWindow | 30 |
| 96 | | *XMM-Newton*/PN | 0600980101 | PrimeFullWindow | 124 |
| 97 | | *NuSTAR*/FPMA,B | 30401033002 | – | 12 |
| 98 | XTE J1829–098 | *XMM-Newton*/PN | 0135746701 | PrimeFullWindow | 1 |
| 99 | | *NuSTAR*/FPMA,B | 90401332002 | - | 55 |
| 100 | XTE J1858 + 034 | *NuSTAR*/FPMA,B | 90501348002 | – | 90 |

This paper has been typeset from a TEX/LATEX file prepared by the author.